Resumming transverse observables for NNLO + PS matching in GENEVA

Alessandro Gavardi,[1] Rebecca von Kuk,[1] and Matthew A. Lim[2,3]
[1]*Deutsches Elektronen-Synchrotron DESY, Notkestr. 85, 22607 Hamburg, Germany*
[2]*Department of Physics and Astronomy, University of Sussex, Sussex House, Brighton, BN1 9RH, United Kingdom*
[3]*Università degli Studi di Milano-Bicocca and INFN Sezione di Milano-Bicocca, Piazza della Scienza 3, Milano 20126, Italy*

(Received 11 December 2025; accepted 30 July 2026; published 11 September 2026)

We study the use of higher-order resummation for transverse observables to achieve NNLO + PS matching within the GENEVA framework. In particular, we embed q_T resummation for color-singlet production at N^{3}LL obtained via soft-collinear effective theory and implemented in the library SCETlib within GENEVA. We also study for the first time the use of the generalized N-jettiness variable in parton shower matching, and achieve the resummation of the one-jettiness defined with transverse measures up to NLL$'$ accuracy. As a case study, we use these resummed calculations to construct a GENEVA NNLO + PS generator for Higgs boson production in heavy-quark annihilation (with beauty or charm quarks in the initial state). The use of transverse measures facilitates the matching to showers ordered in transverse momentum, and opens the door to possible future extensions of this approach to the production of color singlets in association with final-state jets.

DOI: 10.1103/nlfd-2y6w

I. INTRODUCTION

The success of the experimental program at the LHC demands theoretical tools at the highest possible accuracy. While fully differential calculations at fixed-order in perturbation theory have reached N^{3}LO for simple processes [1–4], state-of-the-art for predictions matched to parton shower generators is currently next-to-next-to-leading order (NNLO + PS). Two main approaches exist to achieve this accuracy [5,6], while a third, rather different approach, is currently under active development [7,8].

An interesting question relevant to the construction of NNLO + PS generators concerns the choice of resolution variables, which partition the phase space into jet bins of differing multiplicity and which must be resummed to high logarithmic accuracies. While many choices are in principle possible, the predictions for exclusive observables will depend on said choice, introducing a source of systematic uncertainty. A natural way to gauge the size of this uncertainty would be to compare the predictions of generators constructed using the same method but different variables. In addition, the availability of higher-accuracy parton shower algorithms [9–12] means that one may wish to explore novel variable choices to ensure the preservation of the shower accuracy in matching.

In this work, we implement a new combination of resolution variables in the GENEVA approach. The original formulation of GENEVA [13] used the zero- and one-jettiness [14] to separate the 0/1- and 1/2- jet bins respectively, and indeed many electroweak processes have since been examined in this context [15–21]. The jettiness variable has the advantage of considerable simplicity, admitting a simple factorization structure in SCET-I which facilitates resummation [22,23]. However, the fact that the usual definition of the jettiness involves an invariant masslike measure complicates the matching to commonly employed parton shower algorithms, which tend to be ordered in transverse momentum. An alternative formulation using the color-singlet transverse momentum q_T to separate the 0/1-jet bins was studied in Ref. [24], with q_T resummation at N^{3}LL provided by the RadISH formalism [25,26]. The 1/2-jet separation variable remained, however, the one-jettiness. In Ref. [27], a generator for W^+W^- production was constructed using the hardest and second-hardest jet transverse momenta as variables and SCET-based resummation [28,29]. With these choices, the need for truncated showering techniques [30] in GENEVA was reduced. A summary of the currently available GENEVA implementations is presented in Table II.

The new class of generators we initiate in this work uses transverse observables to separate all jet bins, as in Ref. [27]. As in Ref. [24], we use q_T as the primary resolution variable, though exploiting analytic SCET-II

Published by the American Physical Society under the terms of the Creative Commons Attribution 4.0 International license. Further distribution of this work must maintain attribution to the author(s) and the published article's title, journal citation, and DOI. Funded by SCOAP^3.

resummation provided by SCETlib [31] rather than the RadISH approach previously taken. As a secondary resolution variable, we choose a generalization of the one-jettiness which uses a transverse momentumlike measure. Though the definition of this observable was introduced in the original N-jettiness paper over 15 years ago [14], to our knowledge this is the first time that its resummation has been accomplished beyond leading logarithmic order.[1,2] The observable is interesting not merely because it facilitates matching for color singlet processes, but because of the promise it holds for achieving NNLO + PS matching for color-singlet production in association with additional jets. The work we present here takes a very first step in this direction, achieving NLL′ resummation before the shower matching.

As a case study, we consider the production of a Higgs boson through heavy-quark annihilation ($c\bar{c}, b\bar{b} \to H$). The requisite q_T resummation for this process was achieved at N^{3}LL in Ref. [34], and generators for the $b\bar{b}H$ process were constructed in Refs. [35,36] using the MiNNLOps formalism and approximations for unknown two-loop matrix elements. As detailed in e.g. Ref. [37], measurements of the Higgs boson q_T spectrum could be used in conjunction with precision theory predictions for $b\bar{b}H$ to extract a value for the bottom Yukawa coupling y_b. Generalizations to other color-singlet processes, though time-consuming, are in principle straightforward.

The rest of this paper is arranged as follows. In Sec. II, we provide a brief recap of the GENEVA method for matching NNLO calculations to parton shower, while Sec. III summarises q_T resummation in SCET. In Sec. IV we briefly review the definition of the generalized jettiness for unacquainted readers, before detailing the resummation of a specific choice of measures at NLL′. We present NNLO + PS matched results for $b\bar{b}H$ and $c\bar{c}H$ in Sec. V, before concluding in Sec. VI.

II. THE GENEVA METHOD

The GENEVA method [5,13] relies on defining infrared (IR) safe events at a specific perturbative order, which are obtained by combining fixed-order and resummed calculations. This is achieved by converting IR-divergent final states with M partons into IR-finite final states with N partonic jets, where $M \geq N$, ensuring that the divergences cancel on an event-by-event basis. The conversion is performed using N-jet resolution variables r_N to define slicing parameters r_N^{cut}, which divide the phase space into regions with different numbers of resolved emissions: Φ_0 where there is no additional jet, Φ_1 with one jet and Φ_2 with two or more jets in the final state.

To define the GENEVA differential cross sections with zero, one and two jets, we begin by introducing the following shorthand notation

$$\frac{\mathrm{d}\sigma^{\mathrm{NLO}_0}}{\mathrm{d}\Phi_0}(r_0^{\text{cut}}) = B_0(\Phi_0) + V_0(\Phi_0) + \int \frac{\mathrm{d}\Phi_1}{\mathrm{d}\Phi_0} B_1(\Phi_1)\theta(r_0 < r_0^{\text{cut}}), \quad (1)$$

$$\frac{\mathrm{d}\sigma^{\mathrm{NLO}_1}}{\mathrm{d}\Phi_2}(r_1^{\text{cut}}) = B_1(\Phi_1) + V_1(\Phi_1) + \int \frac{\mathrm{d}\Phi_2}{\mathrm{d}\Phi_1} B_2(\Phi_2)\theta(r_1 < r_1^{\text{cut}}), \quad (2)$$

$$\frac{\mathrm{d}\sigma^{\mathrm{LO}_2}}{\mathrm{d}\Phi_2} = B_2(\Phi_2). \quad (3)$$

where B_M and V_M represent the tree-level and one-loop contributions with M partons in the final state, and we defined

$$\frac{\mathrm{d}\Phi_{N+1}}{\mathrm{d}\Phi_N} = \mathrm{d}\Phi_{N+1}\delta[\Phi_N - \tilde{\Phi}_N(\Phi_{N+1})] \quad (4)$$

to indicate the integration over the Φ_{N+1} phase space points that are projected on Φ_N by the $\tilde{\Phi}_N$ mapping. Following the method first developed in Ref. [27], the differential cross sections with zero, one and two additional jets are then defined as

$$\begin{aligned}
\frac{\mathrm{d}\sigma_0^{\mathrm{MC}}}{\mathrm{d}\Phi_0}(r_0^{\text{cut}}) &= \frac{\mathrm{d}\sigma^{\mathrm{N^3LL}_{r_0}}}{\mathrm{d}\Phi_0}(r_0^{\text{cut}}) - \frac{\mathrm{d}\sigma^{\mathrm{N^3LL}_{r_0}}}{\mathrm{d}\Phi_0}(r_0^{\text{cut}})\bigg|_{\mathrm{NLO}_0} + \frac{\mathrm{d}\sigma^{\mathrm{NLO}_0}}{\mathrm{d}\Phi_0}(r_0^{\text{cut}}) \\
\frac{\mathrm{d}\sigma_1^{\mathrm{MC}}}{\mathrm{d}\Phi_1}(r_1^{\text{cut}}) &= \left\{ \left[\frac{\mathrm{d}\sigma^{\mathrm{N^3LL}_{r_0}}}{\mathrm{d}\Phi_0 \mathrm{d}r_0} - \frac{\mathrm{d}\sigma^{\mathrm{N^3LL}_{r_0}}}{\mathrm{d}\Phi_0 \mathrm{d}r_0}\bigg|_{\mathrm{NLO}_1} \right] \mathcal{P}_{0\to1}(\Phi_1) U_1(\Phi_1, r_1^{\text{cut}}) \right. \\
&\quad \left. + \frac{\mathrm{d}\sigma^{\mathrm{NLO}_1}}{\mathrm{d}\Phi_1}(r_1^{\text{cut}}) + \frac{\mathrm{d}\sigma^{\mathrm{NLL}'_{r_1}}}{\mathrm{d}\Phi_1}(r_1^{\text{cut}}) - \frac{\mathrm{d}\sigma^{\mathrm{NLL}'_{r_1}}}{\mathrm{d}\Phi_1}(r_1^{\text{cut}})\bigg|_{\mathrm{NLO}_1} \right\} \theta(r_0 > r_0^{\text{cut}})
\end{aligned} \quad (5)$$

[1]The NLL resummation should also be achievable within the CAESAR formalism [32], but to our knowledge, this observable has never been studied in that context.

[2]We note that a similar generalization of the jettiness has more recently been proposed in Ref. [33].

$$+\frac{\mathrm{d}\sigma^{\mathrm{LO}_1}_{\mathrm{nonproj}}}{\mathrm{d}\Phi_1}\theta(r_0 < r_0^{\mathrm{cut}}) \tag{6}$$

$$\begin{aligned}\frac{\mathrm{d}\sigma^{\mathrm{MC}}_{\geq 2}}{\mathrm{d}\Phi_2} = &\left\{\left[\frac{\mathrm{d}\sigma^{\mathrm{N^3LL}_{r_0}}}{\mathrm{d}\Phi_0\mathrm{d}r_0} - \frac{\mathrm{d}\sigma^{\mathrm{N^3LL}_{r_0}}}{\mathrm{d}\Phi_0\mathrm{d}r_0}\bigg|_{\mathrm{NLO}_1}\right]\mathcal{P}_{0\to1}(\Phi_1)U_1'(\Phi_1,r_1)\mathcal{P}_{1\to2}(\Phi_2)\right.\\ &\left.+\frac{\mathrm{d}\sigma^{\mathrm{LO}_2}}{\mathrm{d}\Phi_2} + \left[\frac{\mathrm{d}\sigma^{\mathrm{NLL}'_{r_1}}}{\mathrm{d}\Phi_1\mathrm{d}r_1} - \frac{\mathrm{d}\sigma^{\mathrm{NLL}'_{r_1}}}{\mathrm{d}\Phi_1\mathrm{d}r_1}\bigg|_{\mathrm{LO}_2}\right]\mathcal{P}_{1\to2}(\Phi_2)\right\}\theta(r_1 > r_1^{\mathrm{cut}})\theta(r_0 > r_0^{\mathrm{cut}})\\ &+\frac{\mathrm{d}\sigma^{\mathrm{LO}_2}_{\mathrm{nonproj}}}{\mathrm{d}\Phi_2}\theta(r_1 < r_1^{\mathrm{cut}})\theta(r_0 > r_0^{\mathrm{cut}}).\end{aligned} \tag{7}$$

In the above equations, $\mathrm{d}\sigma^{\mathrm{N^3LL}_{r_N},\mathrm{NLL}'_{r_N}}/\mathrm{d}\Phi_N(r_N)$ and $\mathrm{d}\sigma^{\mathrm{N^3LL}_{r_N},\mathrm{NLL}'_{r_N}}/\mathrm{d}\Phi_N\mathrm{d}r_N$ are respectively the cumulant and spectrum of the r_N N^{3}LL or NLL$'$ resummed cross section and the notation $|_{(\mathrm{N})\mathrm{LO}_M}$ indicates their fixed-order expansion at the (N)LO order of the process with M final-state partons. Furthermore, $U_1(\Phi_1, r_1)$ denotes the NLL r_1 Sudakov form factor, $U_1'(\Phi_1, r_1)$ its derivative with respect to r_1, and the functions $\mathcal{P}_{N\to N+1}(\Phi_{N+1})$ (called splitting functions in the GENEVA literature) are used to spread the resummed $\mathcal{T}_N$ spectrum over the Φ_{N+1} phase space. They are defined such that

$$\int\frac{\mathrm{d}\Phi_{N+1}}{\mathrm{d}\Phi_N\mathrm{d}r_N}\mathcal{P}_{N\to N+1}(\Phi_{N+1}) = 1. \tag{8}$$

Finally, the "nonproj" label is used to indicate the Φ_{N+1} phase space points that do not have a Φ_N projection through the $\tilde{\Phi}_N$ mapping.

The $\tilde{\Phi}_1$ mapping is constructed in such a way that it preserves the value of r_0, i.e.

$$r_0(\tilde{\Phi}_1(\Phi_2)) = r_0(\Phi_2), \tag{9}$$

which is crucial to ensure that the r_1 resummation does not spoil the resummed r_0 spectrum. Since we use $r_0 = q_T$ in this work, we require a q_T-preserving mapping in our NLO$_1$ calculation. Mappings which satisfy this criterion have been previously used in Refs. [13,24]. In this work, we construct a new hybrid mapping by combining the ISR part of the $\mathcal{T}_0 - q_T$ preserving mapping from Ref. [13] with the FSR part of the mapping used in Ref. [27] which preserves the transverse momentum of the jet, p_T^{jet}. This has better numerical performance compared to the q_T preserving mapping of Ref. [24] while still avoiding unphysical artefacts in exclusive distributions, which are caused by the FSR part of the $\mathcal{T}_0 - q_T$ mapping.

The integration measure introduced in Eq. (8) is defined as

$$\begin{aligned}\frac{\mathrm{d}\Phi_{N+1}}{\mathrm{d}\Phi_N\mathrm{d}r_N} = &\,\mathrm{d}\Phi_{N+1}\delta[\Phi_N - \bar{\Phi}_N(\Phi_{N+1})]\\ &\times\delta[r_N - r_N(\Phi_{N+1})]\end{aligned} \tag{10}$$

and indicates the integration over the Φ_{N+1} phase space points whose value of the N-jet resolution variable is r_N and which are projected on Φ_N by the $\bar{\Phi}_N$ mapping (called splitting mapping in the GENEVA literature). The $\bar{\Phi}_N$ mapping does not need to coincide with $\tilde{\Phi}_N$. Indeed, to simplify the implementation of the $\mathcal{P}_{1\to2}$ functions, in this work we employ a splitting mapping $\bar{\Phi}_N \neq \tilde{\Phi}_N$, whose details are discussed in Sec. IV C.

III. RESUMMATION OF TRANSVERSE MOMENTUM IN SCET

The factorization of the leading-power q_T spectrum was first established in Refs. [38–40], and extended in Refs. [41–43]. In this paper, we adopt the SCET framework 48–44]], where q_T factorization was formulated in Refs. [49–52]. In particular, we employ rapidity renormalization [51,53] using the exponential regulator [52]. In this formulation, the singular cross section for color-singlet production can be written as

$$\begin{aligned}\frac{\mathrm{d}\sigma^{\mathrm{sing}}}{\mathrm{d}q_T\mathrm{d}\Phi_0} = &\sum_{a,b}H_{ab}(\Phi_0;\mu)\int\mathrm{d}^2\vec{k}_a\mathrm{d}^2\vec{k}_b\mathrm{d}^2\vec{k}_s\\ &\times\delta(q_T - |\vec{k}_a - \vec{k}_b - \vec{k}_s|)B_a(x_a,\vec{k}_a;\mu,\nu/\omega_a)\\ &\times B_b(x_b,\vec{k}_b;\mu,\nu/\omega_b)S_{ab}(\vec{k}_s;\mu,\nu).\end{aligned} \tag{11}$$

The hard function H_{ab} is process-dependent and describes the hard interaction producing the color singlet $ab \to F$, where a, b denote the available partonic channels at leading order. The beam functions $B_{a,b}$ describe collinear radiation with total transverse momentum $\vec{k}_{a,b}$ and longitudinal momentum fractions $x_{a,b} = (m/E_{\mathrm{cm}})e^{\pm Y}$ (for color-singlet mass m, rapidity Y and hadronic center-of-mass energy E_{cm}), with $\omega_{a,b} = x_{a,b}E_{\mathrm{cm}}$. The soft function S_{ab} describes soft radiation with total transverse momentum $\vec{k}_s$. Finally, the scales μ and ν denote the virtuality and rapidity renormalization scales.

To achieve all-order resummation, each of the functions in Eq. (11) is first evaluated at its natural scale(s) $\mu_{H,B,S}$, $\nu_{B,S}$, and then evolved to a common set of scales μ, ν by

solving a coupled system of renormalization group equations. As shown in Ref. [54], the exact solution of said equations in q_T space in terms of distributions is equivalent to the canonical solution in b_T space appropriately transformed. In this work we follow common practice and employ the latter solution. For details see Refs. [54–56].

While the resummed cross section in Eq. (11) is appropriate when describing events at low q_T, for higher values it is no longer adequate and we must rely on a calculation at fixed order in perturbation theory. The matching of resummed and fixed order calculations is achieved additively as detailed in Sec. II—we are still required, however, to specify a prescription which switches off the resummation at large q_T to ensure a smooth transition between the resummed and fixed-order parts of the calculation. This is achieved using hybrid profile scales [57–59], which allow μ_H, μ_B, μ_S to take different values in the resummation region (required to minimise the size of large logarithms), but which flow to a common scale with increasing q_T, thus naturally ending RG evolution for $q_T \sim Q$.

The framework described above is sufficiently general to describe the production of any color-singlet final state (given an appropriate hard function). However, implementation details are in general process-dependent. In particular, the shape of the profile scales which determine the transition between resummation and fixed-order regions of phase space is normally chosen based on the relative size of the singular and nonsingular contributions as a function of q_T and differs between, e.g., Drell-Yan and Higgs boson production. In our specific case of Higgs boson production in heavy-quark annihilation, these considerations were examined in Ref. [34]. Since we directly interface the SCETlib q_T module [60] used in that work to GENEVA, we employ the same central scale choices and profile shapes as used there. We also estimate our uncertainties via profile scale variation in the same manner. We note that just as in Ref. [21], this allows us to separate dependence on the beam and factorization scales μ_B and μ_F, allowing us to perform 7-point scale variations for inclusive observables. For the sake of completeness, we detail our profile scale choices, transition points and variation prescription in Appendix A.

IV. RESUMMATION OF ONE-JETTINESS WITH GENERALIZED MEASURES

A. Observable definition

The N-jettiness observable is most often defined as

$$\mathcal{T}_N = \sum_i \min_m \left\{ \frac{2q_m \cdot p_i}{Q_m} \right\}, \tag{12}$$

where the sum runs over the four-momenta of all colored particles p_i^μ, the minimization over m runs over all beam and jet reference momenta q_m^μ, and the factors Q_m are normalization factors. This definition uses an invariant masslike measure and obeys a SCET-I type factorization, which has been well-studied in the literature.

It was remarked in the original N-jettiness paper, however, that the definition in Eq. (12) can be extended to use generic measures in each beam or jet region [14]. Moreover, N-jettiness can be thought of not merely as an event-shape, but as a way to define an exclusive jet algorithm which partitions the phase space into two beam and N jet regions, to which emissions are assigned. The measure factors which are used to assign emissions to each region need not be identical to the value which the observable returns. In general, therefore, we must define separate distance measures $d_m(p_i)$ which assign the emission i to one of the $N+2$ regions m if

$$d_m(p_i) = \min\{d_1(p_i), \ldots, d_N(p_i), d_a(p_i), d_b(p_i)\}, \tag{13}$$

and the resulting observable f_m which is returned by that emission once it falls into the region m,

$$\mathcal{T}^{(m)} = \sum_{i \in m} f_m(\eta_i, \phi_i) p_{T,i}, \tag{14}$$

where η_i, ϕ_i and $p_{T,i}$ denote the pseudorapidity, azimuth and transverse momentum associated with i. We remark that the definitions of the jet regions d_j for $j \in \{1, \ldots, N\}$ are themselves dependent on a determination of the jet axes, which may be performed either by running an exclusive jet algorithm (e.g. anti-k_T) over the final state, or by a minimization of the N-jettiness over all possible axes. The latter definition has the advantage of guaranteeing insensitivity to soft-recoil effects, whose correct treatment requires the introduction of additional transverse momentum convolutions in the factorization formula. At one-loop, it is equivalent to using the winner-take-all (WTA) axis [61], in that the jet direction is determined solely by the "hardest" emission.

This generalized definition of the N-jettiness has also been well studied in the literature, and the choice of the measures has important consequences for the structure of the factorization. The XCone algorithm implements precisely the procedure described above to act as an exclusive jet algorithm, and in that context a number of different measure choices have been studied [62]. Reference [63] completed the study of factorization types (i.e., all possible combinations of SCET-I/SCET-II measures for beams and jets) and provided the one-loop soft functions relevant for color singlet production in association with a single jet. In addition, the N-subjettiness observable, introduced in Ref. [64] as a way to study jet substructure, uses choices of the f_m which are transverse momentumlike by default.

In this work, we will make specific choices for both the d_m and f_m and use $N = 1$, thus defining a generalized

one-jettiness observable which we refer to as $\mathcal{T}_1^{p_T}$. Specifically, we choose the conical measure [62,65] for the region assignment, which (for isolated jets) clusters in a manner equivalent to the anti-k_T algorithm:

$$d_0(p_i) = 1, \qquad d_{m\geq 1}(p_i) = \frac{R_{im}^2}{R^2}. \tag{15}$$

In the above equation, we have defined a single beam measure,

$$d_0(p_i) = \min\{d_a(p_i), d_b(p_i)\}, \tag{16}$$

and introduced the distance

$$R_{im} \equiv \sqrt{(\eta_i - \eta_m)^2 + (\phi_i - \phi_m)^2} \tag{17}$$

and (constant) jet radius R. For the measurement itself, defining

$$\mathcal{T}_1^{p_T} = \sum_i \begin{cases} p_{T,i} f_B(\eta_i), & \text{for } d_B(p_i) < d_J(p_i), \\ p_{T,i} f_J(\eta_i, \phi_i), & \text{for } d_J(p_i) < d_B(p_i), \end{cases} \tag{18}$$

we choose the boost-invariant generalization of broadening [63,66] for the jet region,

$$\begin{aligned} f_J(\eta_i, \phi_i) &= \sqrt{2\cosh(\eta_i - \eta_J) - 2\cos(\phi_i - \phi_J)} \\ &\equiv \mathcal{R}_{iJ} \end{aligned} \tag{19}$$

where the distance $d_J(p_i)$ is measured with respect to the jet axis J according to Eq. (15), and the transverse energy for the beam region,

$$f_B(\eta_i) = 1, \tag{20}$$

with the distance $d_B(p_i)$ being equal to $d_0(p_i) = 1$. Both observables are of SCET-II type—the setup described above corresponds to one of the choices made in Ref. [63], for which the one-loop soft function was calculated. It was shown in that work that the cross section then factorizes as

$$\begin{aligned} \frac{\mathrm{d}\sigma_\kappa}{\mathrm{d}\Phi_1 \mathrm{d}\mathcal{T}_1^{p_T}} = H_\kappa(\Phi_1, \mu) \int \left(\prod_n \mathrm{d}k_n\right) \\ \times S_\kappa\left(\mathcal{T}_1^{p_T} - \sum_i k_i, \{n_m\}, \{d_m\}, \mu, \frac{\nu}{\mu}\right) \\ \times B_{\kappa_a}\left(k_a, x_a, \mu, \frac{\nu}{\omega_a}\right) B_{\kappa_b}\left(k_b, x_b, \mu, \frac{\nu}{\omega_b}\right) \\ \times J_{\kappa_j}\left(k_j, \mu, \frac{\nu}{\omega_j}\right), \end{aligned} \tag{21}$$

where the channel index $\kappa \equiv \{\kappa_a, \kappa_b, \kappa_j\}$ runs over all possible flavors of incoming and outgoing partons.

B. Ingredients and resummation at NLL′

At NLL′ accuracy, each of the hard, soft, beam and jet functions are required at one-loop accuracy as are the noncusp anomalous dimensions, while the cusp anomalous dimension is needed one order higher. The hard function is easily obtained from the corresponding one-loop QCD amplitude.[3] It satisfies an evolution equation

$$\mu \frac{\mathrm{d}}{\mathrm{d}\mu} \ln H_\kappa(\Phi_1, \mu) = \gamma_H^\kappa(\Phi_1, \mu) \tag{22}$$

where the hard anomalous dimension is of the form

$$\begin{aligned} \gamma_H^\kappa(\Phi_1, \mu) = \Gamma_{\mathrm{cusp}}[\alpha_s(\mu)] \left[\mathbf{T}_a^2 \ln \frac{\omega_a^2 e^{-2\eta_J}}{\mu^2}\right. \\ \left. + \mathbf{T}_b^2 \ln \frac{\omega_b^2 e^{2\eta_J}}{\mu^2} + \mathbf{T}_j^2 \ln \frac{\omega_j^2}{(2\cosh\eta_J)^2 \mu^2}\right] \\ + \gamma_H^\kappa[\alpha_s(\mu)], \end{aligned} \tag{23}$$

$$\gamma_H^\kappa[\alpha_s(\mu)] = (n_q + n_{\bar{q}})\gamma^q[\alpha_s(\mu)] + n_g \gamma^g[\alpha_s(\mu)], \tag{24}$$

where n_q and n_g label respectively the number of quarks and gluons in the channel κ.

The relevant soft function was calculated in Ref. [63]. Its evolution equation reads

$$\begin{aligned} \mu \frac{\mathrm{d}}{\mathrm{d}\mu} S_\kappa\left(k_S, \Phi_1, \mu, \frac{\nu}{\mu}\right) \\ = \int \mathrm{d}k_S' \gamma_{\mu,S}^\kappa\left(k_S - k_S', \Phi_1, \mu, \frac{\nu}{\mu}\right) S_\kappa\left(k_S', \Phi_1, \mu, \frac{\nu}{\mu}\right) \end{aligned} \tag{25}$$

where we have suppressed the dependence on the d_m for brevity and translated the dependence on the reference directions n_m into a dependence on the phase space Φ_1. The soft virtuality anomalous dimension is given to all orders by

$$\begin{aligned} \gamma_{\mu,S}^\kappa\left(k_S, \Phi_1, \mu, \frac{\nu}{\mu}\right) = 2\Gamma_{\mathrm{cusp}}[\alpha_s(\mu)]\delta(k_S) \\ \times \left[-(\mathbf{T}_a^2 + \mathbf{T}_b^2 + \mathbf{T}_j^2)\ln\frac{\nu}{\mu}\right. \\ \left. + \mathbf{T}_j^2 \ln(2\cosh\eta_J) + (\mathbf{T}_a^2 - \mathbf{T}_b^2)\eta_J\right] \\ + \gamma_{\mu,S}^\kappa[\alpha_s(\mu)]\delta(k_S) \end{aligned} \tag{26}$$

[3]Although in general both hard and soft functions are matrices in color space, for the case of $N = 1$ the color algebra diagonalizes and it is possible to rewrite the factorization in the form Eq. (21).

where the noncusp term $\gamma^{\kappa(0)}_{\mu,S}[\alpha_s(\mu)] = 0$ at one-loop. The soft function also obeys a rapidity evolution equation

$$\nu\frac{\mathrm{d}}{\mathrm{d}\nu}S_\kappa\left(k_S,\Phi_1,\mu,\frac{\nu}{\mu}\right) = \int \mathrm{d}k'_S\gamma^{\kappa}_{\nu,S}(k_S-k'_S,\mu)S_\kappa\left(k'_S,\Phi_1,\mu,\frac{\nu}{\mu}\right) \quad (27)$$

where the rapidity anomalous dimension at one-loop order is given by

$$\gamma^{\kappa(1)}_{\nu,S}(k_S,\mu) = 2\Gamma_0\frac{\alpha_s(\mu)}{4\pi}\left[(\mathbf{T}_a^2+\mathbf{T}_b^2+\mathbf{T}_j^2)\frac{1}{\mu}\mathcal{L}_0\left(\frac{k_S}{\mu}\right)\right] \quad (28)$$

and the plus distribution $\mathcal{L}_0(x)$ is defined as in Appendix B.

The collinear beam functions relevant for the observable are those calculated at one-loop in e.g. Refs. [28,67,68] while the recoil-free broadening jet function was calculated in Ref. [61]. Both beam and jet functions obey a set of similar evolution equations,

$$\mu\frac{\mathrm{d}}{\mathrm{d}\mu}B_i\left(k_B,x,\mu,\frac{\nu}{\omega}\right) = \int \mathrm{d}k'_B\gamma^i_{\mu,B}\left(k_B-k'_B,\mu,\frac{\nu}{\omega}\right)B_i\left(k'_B,x,\mu,\frac{\nu}{\omega}\right), \quad (29)$$

$$\nu\frac{\mathrm{d}}{\mathrm{d}\nu}B_i\left(k_B,x,\mu,\frac{\nu}{\omega}\right) = \int \mathrm{d}k'_B\gamma^i_{\nu,B}(k_B-k'_B,\mu)B_i\left(k'_B,x,\mu,\frac{\nu}{\omega}\right), \quad (30)$$

$$\mu\frac{\mathrm{d}}{\mathrm{d}\mu}J_i\left(k_J,\mu,\frac{\nu}{\omega}\right) = \int \mathrm{d}k'_J\gamma^i_{\mu,J}\left(k_J-k'_J,\mu,\frac{\nu}{\omega}\right)J_i\left(k'_J,\mu,\frac{\nu}{\omega}\right), \quad (31)$$

$$\nu\frac{\mathrm{d}}{\mathrm{d}\nu}J_i\left(k_J,\mu,\frac{\nu}{\omega}\right) = \int \mathrm{d}k'_J\gamma^i_{\nu,J}(k_J-k'_J,\mu)J_i\left(k'_J,\mu,\frac{\nu}{\omega}\right), \quad (32)$$

where the virtuality anomalous dimensions take the forms

$$\gamma^i_{\mu,B}\left(k_B,\mu,\frac{\nu}{\omega}\right) = \left\{2\mathbf{T}_i^2\Gamma_{\mathrm{cusp}}\log\frac{\nu}{\omega}+\gamma^i_B[\alpha_s(\mu)]\right\}\delta(k_B), \quad (33)$$

$$\gamma^i_{\mu,J}\left(k_J,\mu,\frac{\nu}{\omega}\right) = \left\{2\mathbf{T}_i^2\Gamma_{\mathrm{cusp}}\log\frac{\nu}{\omega}+\gamma^i_J[\alpha_s(\mu)]\right\}\delta(k_J), \quad (34)$$

and at one loop $\gamma^{i(0)}_{B/J}[\alpha_s(\mu)] = -2\gamma^{i(1)}[\alpha_s(\mu)]$. The one-loop rapidity anomalous dimensions are instead given by

$$\gamma^i_{\nu,B}(k_B,\mu) = -2\Gamma_0\frac{\alpha_s(\mu)}{4\pi}\mathbf{T}_i^2\frac{1}{\mu}\mathcal{L}_0\left(\frac{k_B}{\mu}\right) \quad (35)$$

$$\gamma^i_{\nu,J}(k_J,\mu) = -2\Gamma_0\frac{\alpha_s(\mu)}{4\pi}\mathbf{T}_i^2\frac{1}{\mu}\mathcal{L}_0\left(\frac{k_J}{\mu}\right). \quad (36)$$

The evolution equations in μ and ν are most easily solved by transforming to Laplace space, first evolving from $\nu_X \to \nu$ at fixed μ_X and subsequently from $\mu_X \to \mu$ (for $X \in \{B,S,J\}$). At NLL, the solution for the soft function can be written analytically as

$$S_\kappa\left(k_S,\Phi_1,\mu,\frac{\nu}{\mu}\right) = \exp\left\{2(C_{\kappa_a}+C_{\kappa_b}+C_{\kappa_j})K_\Gamma(\mu_S,\mu)+\left[2(C_{\kappa_a}-C_{\kappa_b})\eta_J+2C_{\kappa_j}\ln(2\cosh\eta_J)+2(C_{\kappa_a}+C_{\kappa_b}+C_{\kappa_j})\ln\frac{\mu_S}{\nu}\right]\eta_\Gamma(\mu_S,\mu)\right\} \times \int \mathrm{d}k'_S\mathcal{V}_{\eta^\kappa_S}(k_S-k'_S,\mu_S)S_\kappa\left(k'_S,\Phi_1,\mu_S,\frac{\nu_S}{\mu_S}\right), \quad (37)$$

$$\eta^\kappa_S = \frac{\alpha_s(\mu_S)}{4\pi}2\Gamma_0(C_{\kappa_a}+C_{\kappa_b}+C_{\kappa_j})\ln\left(\frac{\nu}{\nu_S}\right), \quad (38)$$

where the function $\mathcal{V}_a(k,\mu)$ is defined in Appendix B and the quadratic Casimir factors $C_i = \mathbf{T}_i^2$. Similarly, the solution for the beam and jet functions can be written as

$$B_i\left(k_B, x, \mu, \frac{\nu}{\omega}\right) = \exp\left\{K_\gamma(\mu_B, \mu) + 2C_i \ln\frac{\nu}{\omega}\eta_\Gamma(\mu_B, \mu)\right\} \int \mathrm{d}k'_B \mathcal{V}_{\eta^i_B}(k_B - k'_B, \mu_B) B_i\left(k'_B, x, \mu_B, \frac{\nu_B}{\mu_B}\right), \tag{39}$$

$$\eta^i_B = -\frac{\alpha_s(\mu_B)}{4\pi} 2\Gamma_0 C_i \ln\left(\frac{\nu}{\nu_B}\right), \tag{40}$$

$$J_i\left(k_J, \mu, \frac{\nu}{\omega}\right) = \exp\left\{K_\gamma(\mu_J, \mu) + 2C_i \ln\frac{\nu}{\omega}\eta_\Gamma(\mu_J, \mu)\right\} \int \mathrm{d}k'_J \mathcal{V}_{\eta^i_J}(k_J - k'_J, \mu_J) J_i\left(k'_J, \mu_J, \frac{\nu_J}{\mu_J}\right), \tag{41}$$

$$\eta^i_J = -\frac{\alpha_s(\mu_J)}{4\pi} 2\Gamma_0 C_i \ln\left(\frac{\nu}{\nu_J}\right). \tag{42}$$

For convenience, we reproduce the one-loop expressions for soft, beam and jet functions in Appendix C. We note that while it is possible to write down the solutions of the evolution equations analytically at NLL (NLL′) order, extending the above solutions to higher resummed orders seems challenging. The underlying reason for this is a combination of the facts that the evolution equations are solved in Laplace space and that the rapidity anomalous dimensions have a nontrivial dependence on $k_{B,S,J}$. At one-loop order, this necessitates taking an inverse Laplace transform of functions of the form $\exp(-a \ln x)$, for constant a. While this is still possible analytically at this order, the appearance of higher powers of the logarithm in the exponent (arising ultimately from higher plus distributions $\mathcal{L}_{1,2,\ldots}$ in γ_ν) hinders an analytic treatment starting at NNLL. Resummation at this order is therefore likely to require a numerical implementation of the inverse integral transform, as is normally performed for q_T resummation.

C. Splitting mappings

To generate hard events that are distributed according to the NLL′ $\mathcal{T}_1^{p_T}$ resummed spectrum, GENEVA assigns the events a weight obtained by multiplying the spectrum by a function (called splitting function in the GENEVA literature) of the $\mathrm{d}\Phi_2$ phase space that integrates to 1 for every underlying Φ_1 phase space point and $\mathcal{T}_1^{p_T}$ value:

$$\int \frac{\mathrm{d}\Phi_2}{\mathrm{d}\Phi_1 \mathrm{d}\mathcal{T}_1^{p_T}} \mathcal{P}_{1\to2}(\Phi_2) = 1. \tag{43}$$

The details of the numeric implementation and the functional forms of the splitting functions used by GENEVA are provided in Refs. [21,69].

This procedure requires introducing a projection $\bar{\Phi}_1$ (called a splitting mapping in the GENEVA literature) from the phase space $\mathrm{d}\Phi_2$ to the underlying phase space $\mathrm{d}\Phi_1$. The choice of such a projection is constrained by the requirement of infrared safety that univocally fixes the splitting mapping in the limit of small $\mathcal{T}_1^{p_T}$. At large $\mathcal{T}_1^{p_T}$, instead, the choice is largely arbitrary, to the point that not all the phase space points are even required to be projectable (a nonprojectable Φ_2 phase space point would simply imply that $P_{1\to2}(\Phi_2) = 0$). The arbitrariness of this choice might appear to translate into a large theoretical uncertainty in the final distributions. This, however, is not the case, since the splitting functions always multiply differences between resummed spectra and their truncated perturbative expansion, which, at large values of $\mathcal{T}_1^{p_T}$, are beyond the accuracy of the calculation. In other words, different choices of splitting mappings introduce distortions in the distributions of the generated events, whose size is formally subleading with respect to the claimed NNLO accuracy.

For some distributions of particular importance, however, it might be preferable to avoid these kinds of effects entirely. To that purpose, we can exploit the freedom in the choice of the mapping to enforce the preservation of a set of observables O_i, for which

$$O_i(\Phi_2) = O_i(\bar{\Phi}_1(\Phi_2)). \tag{44}$$

For these observables, the $\mathcal{T}_1^{p_T}$ resummation can be implemented in a unitary fashion, such that their distributions remain unaffected.

In this work, we require the splitting mapping to preserve the entire color singlet four-momentum. This guarantees that the NNLO accuracy of the Higgs rapidity distribution and the N^{3}LL′ accuracy of the Higgs transverse momentum distribution are not spoiled. This condition still leaves one degree of freedom that we fix with the further constraint that the splitting mapping also preserves the rapidity of the "hardest" final-state parton (i.e., the one that defines the jet direction in the WTA clustering). The choice of $\mathcal{T}_1^{p_T}$ as 1-jet resolution variable does not constrain the mapping, but affects the numeric implementation of the splitting functions. Guaranteeing that Eq. (44) is satisfied indeed requires an analytic computation of the integration limits on Φ_2 at fixed $\Phi_1 = \bar{\Phi}_1(\Phi_2)$ and $\mathcal{T}_1^{p_T}$, as well as the measure $\mathrm{d}\Phi_2/\mathrm{d}\Phi_1\mathrm{d}\mathcal{T}_1^{p_T}$.

V. RESULTS

In this section, we present our numerical results for the $q\bar{q} \to H$ process in a proton-proton scattering. We use the following input parameters: $E_{\mathrm{cm}} = 13$ TeV, Higgs boson

mass $m_H = 125$ GeV and strong coupling $\alpha_s(m_Z) = 0.118$ with $m_Z = 91.1876$ GeV. Unless otherwise indicated we use the MSHT20nnlo PDF set [70]. The Yukawa couplings are computed by evolving the $\overline{\text{MS}}$ quark masses $\bar{m}_q(m_q)$ to the desired scale. The input values are $\bar{m}_b(\bar{m}_b) = 4.18$ GeV and $\bar{m}_c(\bar{m}_c) = 1.27$ GeV [71]. Finally, we set the Higgs vacuum expectation value to $v = 246.22$ GeV.

A. Fixed order validation

We begin by validating our results at fixed order in perturbation theory. Before presenting our numerical comparisons, we take this opportunity to remind the reader of a subtlety in choosing the renormalization scale in a resummed calculation, which will affect our results. The profile scales which we employ in GENEVA are functions of the resolution variable q_T. The consequence of this is that the operations of setting the scale and integrating the q_T spectrum to obtain the total cross section (or an inclusive distribution such as the color singlet rapidity) do not commute. This leaves some freedom in how we present our results—we can either set scales in the spectrum and obtain inclusive quantities by integration, or instead set scales in the integrated cross section and obtain the spectrum by differentiation. The two options differ by formally higher-order terms, which however can be numerically sizeable. The first choice is more natural when one is interested in the q_T spectrum, since it matches what one would normally do in a resummed calculation. The latter instead guarantees that the results of a fixed order calculation (say, the NNLO cross section) are recovered, but may result in distortions of the q_T spectrum.

In Ref. [13], a compromise was proposed. The key idea is to set scales in the spectrum, but to add back a higher-order term which is given by the difference of the spectrum and the q_T-derivative of the cumulant. This is further modulated by an interpolating function $\kappa(q_T)$, which limits the activity of the term to the small q_T region. In this way, one obtains the correct fixed order normalization for inclusive quantities while minimizing any distortions of the q_T spectrum. In this work, we have chosen not to adopt this approach. For the $b\bar{b} \to H$ process in particular, the difference between spectrum and cumulant scale setting is a numerically large effect (in contrast to e.g. Drell-Yan, see Appendix E), and our predictions would be extremely sensitive to the exact way in which the cross section fix was implemented. In the rest of this subsection, we have set scales in the cumulant (which facilitates the comparison of our results with fixed order codes). In following subsections, however (and in particular when examining exclusive distributions such as the q_T spectrum), we have instead adopted spectrum scale setting. This is in general more appropriate for Higgs boson production in heavy-quark fusion, since measurements of the Higgs boson q_T spectrum are likely to be one of the few ways in which this process can be probed—spectrum scale setting will therefore lead to the "best" description for this observable.

TABLE I. Comparison between SusHi and GENEVA of predictions for the NNLO total cross section in $b\bar{b} \to H$. GENEVA predictions at various values of q_T^{cut} are shown, and at various values of $\mu = \mu_R = \mu_F$.

$\sigma^{\text{NNLO}}_{b\bar{b}\to H}$ [fb]	SusHi	$q_T^{\text{cut}} = 1$ GeV	$q_T^{\text{cut}} = 5$ GeV	$q_T^{\text{cut}} = 10$ GeV
$\mu = m_H$	543.5 ± 0.5	544.3 ± 1.0	544.9 ± 0.8	548.6 ± 0.4
$\mu = m_H/2$	518.0 ± 0.5	518.5 ± 1.1	517.8 ± 0.8	518.4 ± 0.5
$\mu = 2m_H$	581.7 ± 0.6	583.3 ± 0.9	585.1 ± 0.7	591.4 ± 0.4

The GENEVA predictions for the inclusive cross section at various values of q_T^{cut} are shown in Table I, and compared to NNLO predictions obtained from SusHi [72]. The absence of a fully local NNLO subtraction means that the implementation of Eq. (5) in GENEVA is done only in an approximate fashion, dropping all fixed order NNLO terms and relying on the singular approximation to the cross section at leading power to provide the two-loop information [13,15]. This is exactly equivalent to an NNLO calculation in the limit $q_T^{\text{cut}} \to 0$; however, for finite values one misses $\mathcal{O}(\alpha_s^2)$ power corrections below q_T^{cut}. It is therefore desirable to set the cut as small as possible to minimise the effect of these inclusive nonsingular terms. The differences we observe with respect to the exact calculation implemented in SusHi are minor, reaching only 1% even at very large values $q_T^{\text{cut}} = 10$ GeV: moreover, for $q_T^{\text{cut}} = 1$ GeV the GENEVA cross section is equivalent to that returned by SusHi to within the statistical precision of the calculation ($\sim$0.2%). In the following we therefore will use $q_T^{\text{cut}} = 1$ GeV as our default choice. We also remark that, as in several previous implementations of GENEVA for color singlet production [21,24,27], we do not need to employ a reweighting procedure to account for missing nonsingular terms below r^{cut}. This need has in any case been recently obviated by the development of improved subtraction techniques in GENEVA, which combine the projection-to-Born method with slicing to allow very small values of r^{cut} to be reached while correctly accounting for fiducial power corrections [73].

In Fig. 1 we validate our predictions for the NNLO Higgs boson rapidity spectrum against an independent calculation from MCFM, obtained using zero-jettiness slicing [74,75]. Note that compatibility with MCFM requires us to set in this case (and in this case alone) $\mu_F = m_H/4, \mu_R = m_H$ and to use the CT14NNLO PDF set [76]. We observe excellent agreement between the two calculations, both for the central value and for the 7-point scale variation bands.

B. Resummed validation

The GENEVA method relies on an additive matching procedure of resummed and fixed-order calculations. It should therefore be the case that predictions for the $0-$ jet

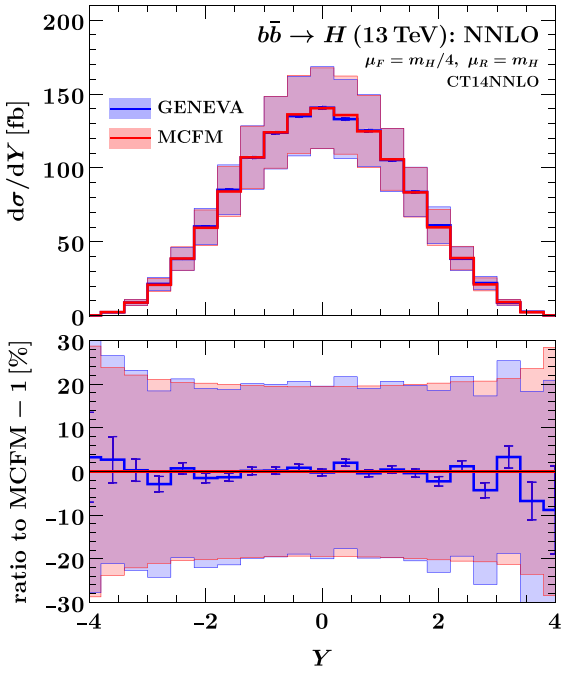


FIG. 1. Comparison between MCFM and GENEVA for the NNLO Higgs boson rapidity spectrum in $b\bar{b} \to H$. Uncertainty bands are obtained via a 7-pt. scale variation procedure.

resolution variable (in this case, q_T) from the event generator are exactly N^{3}LL accurate by construction, at least at parton level. In Fig. 2 we confirm this explicitly by

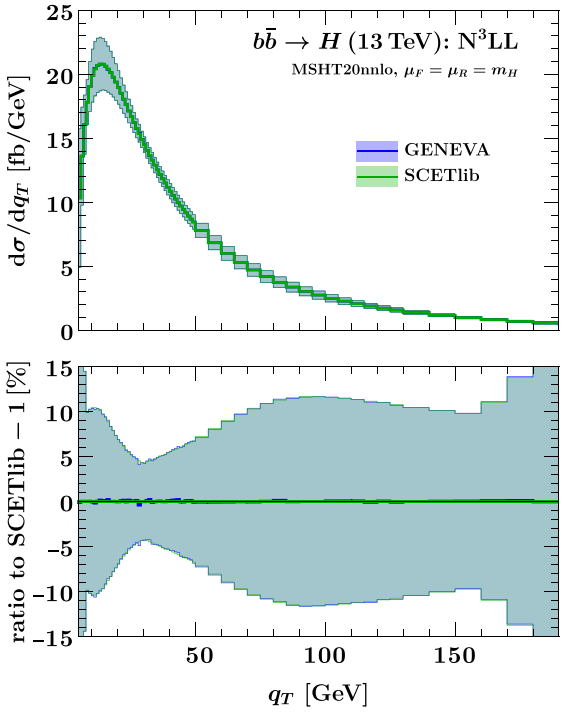


FIG. 2. Comparison between SCETlib and GENEVA for the N^{3}LL Higgs boson q_T spectrum in $b\bar{b} \to H$. Uncertainty bands are obtained as explained in Appendix A.

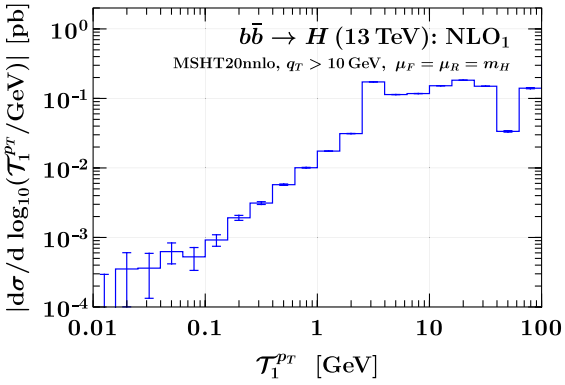


FIG. 3. Nonsingular $\mathcal{T}_1^{p_T}$ spectrum for $b\bar{b} \to H$.

comparison with a separate run of SCETlib. We observe complete agreement for both central value and uncertainty bands, thus corroborating the correctness of our implementation.

C. The 1/2 – jet bin separation

A novel feature of this work is the use of $\mathcal{T}_1^{p_T}$ as a resolution variable to separate the 1- and 2-jet bins. We remind the reader that, in addition to the resummation of this variable at NLL′, the implementation of this variable in the event generator has required us to develop appropriate mappings for the splitting functions which spread the resummation over the higher multiplicity phase space. Both issues are detailed in Sec. IV.

In Fig. 3 we verify that our implementation of Eq. (21) does indeed have the correct logarithmic structure in the $\mathcal{T}_1^{p_T} \to 0$ limit. We plot the nonsingular difference between the leading power expansion of the factorization formula and an exact fixed-order calculation at NLO$_1$ accuracy (where the subscript indicates the number of final state partons). We observe that the double logarithmic plot correctly shows a linear suppression of the nonsingular remnant, which approaches zero with falling $\mathcal{T}_1^{p_T}$. Figure 4 shows the resummed $\mathcal{T}_1^{p_T}$ distribution at NLL′ accuracy (for $q_T > 10$ GeV), which exhibits the characteristic Sudakov peak. In the following, we will set the value of $(\mathcal{T}_1^{p_T})^{\text{cut}}$ appearing in the 1- and 2-jet GENEVA differential cross sections of Eqs. (6) and (7) to 1 GeV, and the jet radius R appearing in Eq. (15) to 0.4.

D. Effect of showering

One of the advantages of using $\mathcal{T}_1^{p_T}$ instead of $\mathcal{T}_1$ as 1-jet resolution variable is that it facilitates the matching to showers ordered in transverse momentum.[4] In this work, we shower the partonic events with the p_T-ordered PYTHIA8

[4]In particular the clustering done according to Eqs. (13) and (18) is equivalent to the anti-k_T algorithm. This greatly reduces the number of shower histories that get vetoed in the matching procedure.

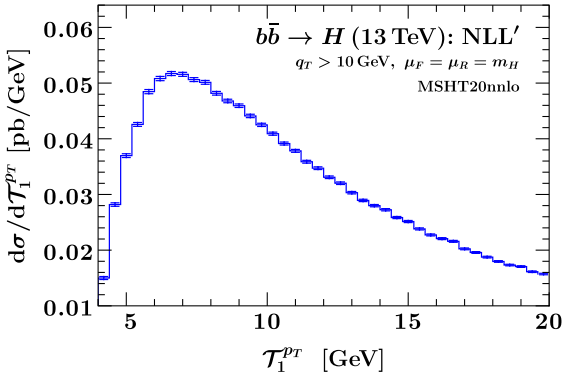


FIG. 4. Resummed $\mathcal{T}_1^{p_T}$ spectrum for $b\bar{b} \to H$.

shower [77], after setting the option `SpaceShower:dipoleRecoil=on` [78,79]. This parameter ensures that the recoil momentum of ISR emissions is distributed within the color dipole whenever kinematically possible (for FSR emissions, this is the default behavior), thus reducing the impact of the shower on the color singlet momentum. In previous work, this was shown to improve the agreement between parton-level and showered predictions for the color-singlet transverse momentum [17,24]. The choice of recoil scheme can significantly affect the accuracy of PSs and may lead to spurious contributions at NLL [9,80–84]. In this work, however, we take the PS to set the (LL) accuracy of our predictions and leave a detailed study to future work.

In Fig. 5, we show the effect of showering on the sole inclusive and differential quantity for $b\bar{b} \to H$, i.e. the Higgs boson rapidity. We observe that, as expected, the shower does not alter the distribution.

Moving to more exclusive quantities, in Figs. 6 and 7 we show the Higgs boson q_T spectrum in $b\bar{b} \to H$ and $c\bar{c} \to H$ respectively, again comparing parton-level predictions with

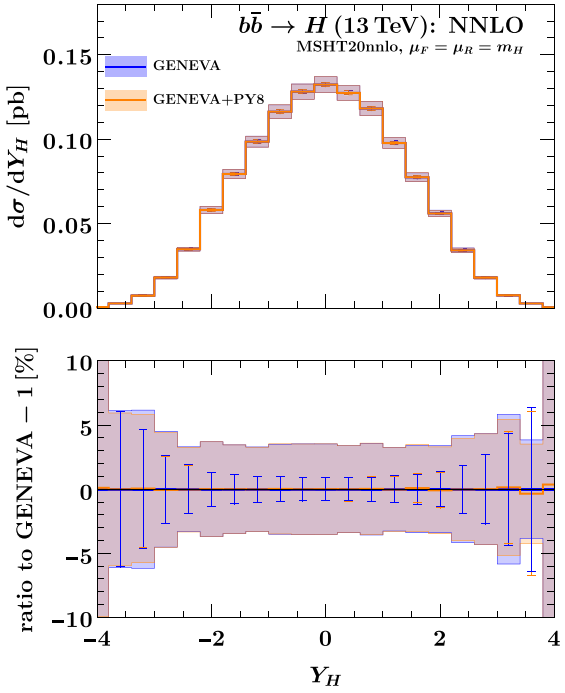


FIG. 5. Higgs boson rapidity spectrum in $b\bar{b} \to H$. Results are shown at parton level and after showering.

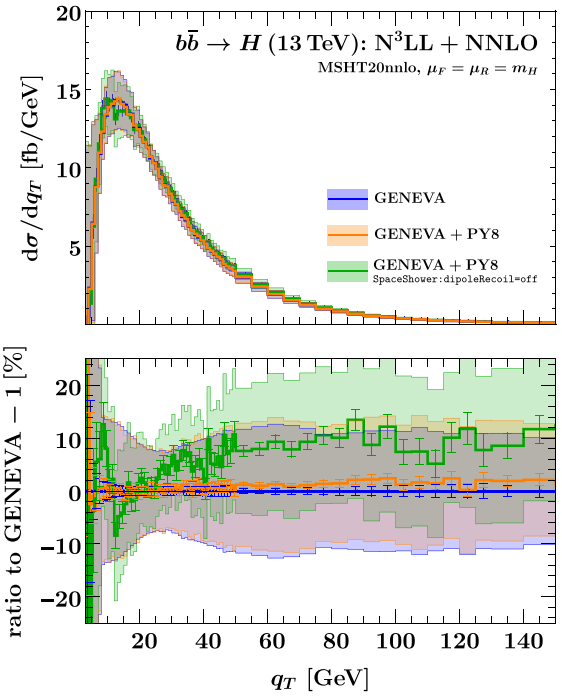


FIG. 6. Higgs boson q_T spectrum in $b\bar{b} \to H$. Results are shown at parton level and after showering.

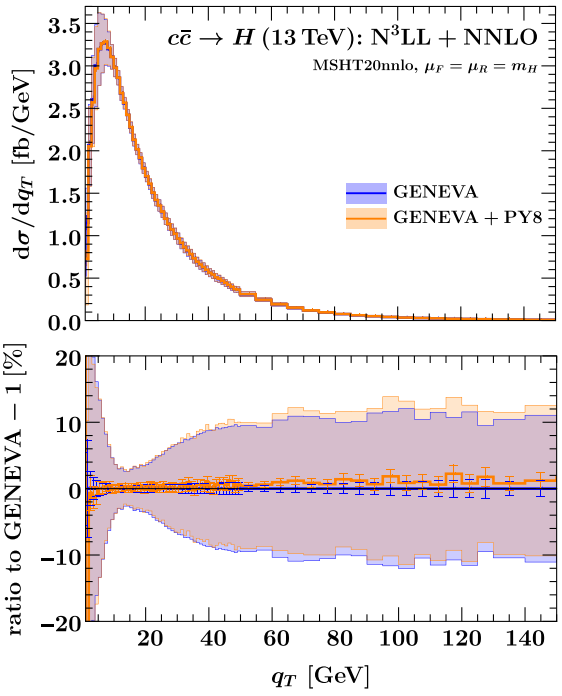


FIG. 7. As in Fig. 6, but for $c\bar{c} \to H$.

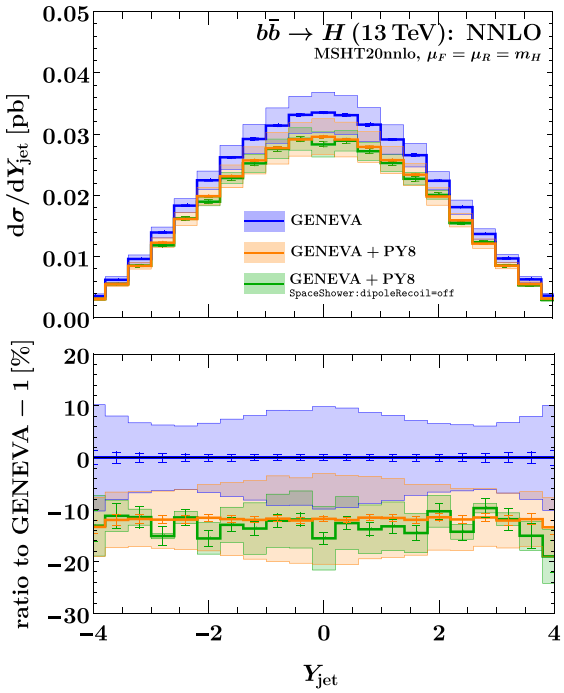


FIG. 8. Hardest jet rapidity spectrum in $b\bar{b} \to H$. Results are shown at parton level and after showering.

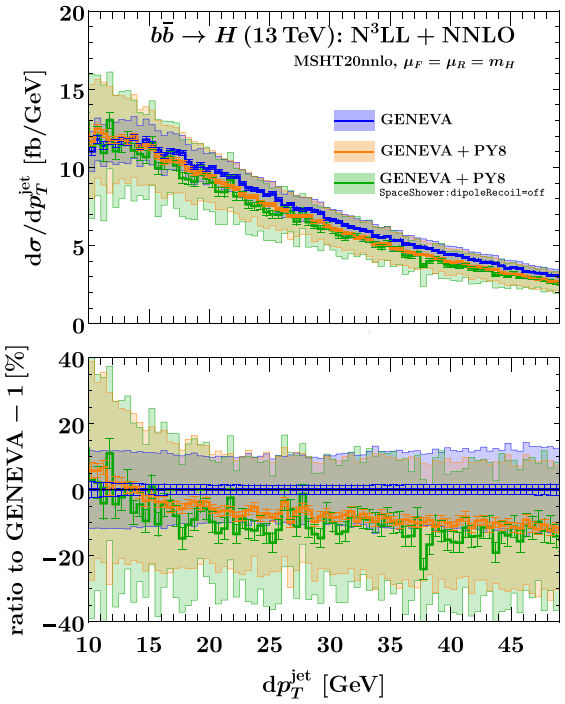


FIG. 9. Hardest jet p_T spectrum in $b\bar{b} \to H$. Results are shown at parton level and after showering.

those after showering. For completeness, we also show the q_T spectrum in $b\bar{b} \to H$ with the option `SpaceShower:dipoleRecoil=off` (green) in Fig. 6. In this case, we observe deviations of up to 10% in the central value compared to the partonic results. Nevertheless, the two options remain consistent within the scale uncertainties. For the more local recoil scheme, we observe extremely good agreement between our partonic results shown in blue (which are formally N^{3}LL + NNLO accurate) and our showered results in orange.

In Figs. 8 and 9, we show the rapidity and transverse momentum of the hardest jet in $b\bar{b} \to H$, respectively. In both the figures, the hardest jet is defined as the jet with the largest transverse momentum obtained clustering the final-state partons with an anti-k_T jet algorithm with jet radius $R = 0.4$. Furthermore, in Fig. 8, jets are required to have a minimum transverse momentum of 30 GeV. The effect of showering on these exclusive distributions is greater, reaching up to ∼15% on the central value but can be understood from its radiation pattern. In the p_T^{jet} spectrum, we observe a depletion in the high-p_T^{jet} tail, which arises from additional radiation generated by the shower that redistributes energy among the final-state partons and reduces the transverse momentum of the leading jet. This behavior also impacts the rapidity distribution when imposing the requirement $p_T^{\text{jet}} > 30$ GeV on the hardest jet. In this region, the showered prediction lies below the partonic result, which means that fewer events pass the cut after showering, leading to a reduced overall differential cross section in the rapidity spectrum.

VI. CONCLUSIONS

In this work we have investigated the use of transverse resolution variables to achieve NNLO + PS matching within the GENEVA framework. In particular, we combine q_T resummation at N^{3}LL, obtained via an interface to the SCETlib library, with $\mathcal{T}_1^{p_T}$ resummation at NLL′. This combination of variables facilitates matching to transverse momentum ordered showers while also providing high accuracy predictions for the color singlet transverse momentum. We have tested our framework on Higgs boson production in heavy-quark annihilation, in particular examining the $b\bar{b} \to H$ channel, finding good agreement with independent fixed order calculations and verifying that the q_T distribution is numerically preserved after showering, even though the formal logarithmic accuracy of the showered events remains limited by the shower LL accuracy.

A possible direction for future work would be to compare the results of this calculation with those obtained using a different resummation variable, which could provide useful insights into the estimation of the theoretical uncertainties. Even though the GENEVA framework permits the use of different resummation variables, the switch between them has not yet been automated and requires a dedicated implementation for each process. To get a sense of the expected size of the effect, one could look at the comparison between q_T and $\mathcal{T}_0$ resummation performed for the Drell-Yan process in ref. [24] (see Figs. 8–10). In this case, one observes an $\mathcal{O}(10\%)$ effect across most of the

spectra with larger differences at small values of the resummation variables (in particular in the $\mathcal{T}_0$ distribution, where they are not covered by the theoretical uncertainties estimated using scale variations).

Moreover, the methods developed here could be extended to the production of other color singlet processes. This could for example be useful in the context of M_W extractions—for example, in Ref. [85], differential distributions for W and Z boson production obtained using the MiNNLOps generator [6] are reweighted to $\mathrm{N^3LL+NNLO}$ accuracy with SCETlib. Extending the generators we have developed here to the Drell-Yan case would remove the need for this reweighting step, since we interface SCETlib directly and reach $\mathrm{N^3LL+NNLO}$ accuracy in the q_T distribution by construction.

Another interesting direction to pursue is the extension of the resummation accuracy in $\mathcal{T}_1^{p_T}$ to NNLL′. This would allow matching fixed-order calculations for color singlet production in association with a hard jet to parton shower algorithms. Although at present the most promising route to this goal seems to be using the normal, invariant mass definition of the one-jettiness (and indeed, both the required fixed-order and resummed calculations for the $Z+j$ process are now implemented in GENEVA [73,86]), as in the color singlet case the transverse nature of $\mathcal{T}_1^{p_T}$ is likely to facilitate matching to transverse momentum-ordered showers. Extension of the resummation accuracy would require the computation of an appropriate 2-loop soft function, which could for example be achieved using SoftSERVE [87–89].

Finally, an important topic in perturbative calculations is the consistent estimation of theoretical uncertainties related to missing higher orders. Approaches based on theory nuisance parameters (TNPs) have shown promise in both resummed and fixed order calculations [90,91] and how similar techniques could be applied to the event generation case is an interesting open question. The fact that a direct application of the TNP approach to the resummed q_T spectrum has already been presented in Ref. [90] perhaps suggests that generators of the kind we have presented in this work (using SCET-based resummation and q_T as resolution variable) may provide a starting point. We leave this to future work.

ACKNOWLEDGMENTS

We are grateful to Ciaran Williams for providing the NNLO predictions for $b\bar{b}\to H$ from MCFM which were used in our validation. We thank Simone Alioli, Andrea Banfi, Alessandro Broggio, Johannes Michel and Frank Tackmann for useful discussions, and Thomas Cridge for early collaboration on this project. We also thank our other GENEVA and SCETlib collaborators for their work on the code. This project has received funding from the European Research Council (ERC) under the European Union's Horizon 2020 research and innovation program (Grant Agreement No. 101002090 COLORFREE).

DATA AVAILABILITY

The data that support the findings of this article are not publicly available. The data are available from the authors upon reasonable request.

APPENDIX A: PROFILE SCALES AND SCALE VARIATION

The canonical boundary scales in b_T space are given by

$$\begin{aligned}
&\text{virtuality}: \quad \mu_H = m_H, \quad \mu_B = b_0/b_T, \quad \mu_S = b_0/b_T,\\
&\qquad\qquad\quad \mu_f = b_0/b_T, \quad \mu_0 = b_0/b_T,\\
&\text{rapidity}: \quad \nu_B = m_H, \quad \nu_S = b_0/b_T,
\end{aligned} \tag{A1}$$

where $b_0 \equiv 2e^{-\gamma_E} \approx 1.12291$, μ_H, (μ_B,ν_B), and (μ_S,ν_S) are the boundary scales for the hard, beam, and soft functions, and μ_f is the scale at which the PDFs inside the beam functions are evaluated. The rapidity anomalous dimension must also be resummed and μ_0 is its associated boundary scale. Evolution of each of the functions in Eq. (11) from these scales to common scales μ,ν resums all canonical b_T-space logarithms $\ln^n[(b_0/b_T)/m_H]$. The corresponding resummed result in q_T space is then obtained via inverse Fourier transform.

Choosing scales which are functions of the variable being resummed facilitates deactivation of the resummation in the fixed-order region of phase space. We choose hybrid profile scales, depending on both b_T and q_T, as

$$\begin{aligned}
&\mu_H = \nu_B = \mu_{\mathrm{FO}} = m_H,\\
&\mu_X = m_H f_{\mathrm{run}}\left[\frac{q_T}{m_H}, \frac{1}{m_H}\mu_*\left(\frac{b_0}{b_T}, \mu_X^{\mathrm{min}}\right)\right],\\
&\mu_0 = \mu_*\left(\frac{b_0}{b_T}, \mu_0^{\mathrm{min}}\right),
\end{aligned} \tag{A2}$$

where $\mu_X \in \{\mu_B,\mu_S,\nu_S,\mu_f\}$. The function μ_* specifies our nonperturbative prescription, which prevents the beam and soft scales reaching values $1/b_T \lesssim \Lambda_{\mathrm{QCD}}$ and allows the inverse Fourier transform to q_T space to be performed. It is given by

$$\mu_*(x,y) = \sqrt{x^2+y^2} \tag{A3}$$

f_{run} is the hybrid profile function given by [59]

$$f_{\mathrm{run}}(x,y) = 1 + g_{\mathrm{run}}(x)(y-1), \tag{A4}$$

where $g_{\mathrm{run}}(x)$ determines the transition as a function of $x = q_T/m_H$,

$$g_{\rm run}(x) = \begin{cases} 1 & 0 < x \le x_1, \\ 1 - \frac{(x-x_1)^2}{(x_2-x_1)(x_3-x_1)} & x_1 < x \le x_2, \\ \frac{(x-x_3)^2}{(x_3-x_1)(x_3-x_2)} & x_2 < x \le x_3, \\ 0 & x_3 \le x, \end{cases} \tag{A5}$$

with transition points x_i for $i \in \{1,2,3\}$. The parameters x_1 and x_3 determine the start and end of the transition and $x_2 = (x_1 + x_3)/2$ corresponds to the turning point. We use $[x_1, x_2, x_3] = [0.1, 0.45, 0.8]$ as our central values.

The profile scales are varied as follows:

$$\begin{aligned} \mu_H &= \mu_{\rm FO} = 2^{w_{\rm FO}} m_H, \\ \nu_B &= \mu_{\rm FO} f_{\rm vary}^{v_{\nu_B}}\left(\frac{q_T}{m_H}\right), \\ \mu_X &= \mu_{\rm FO} f_{\rm vary}^{v_{\mu_X}}\left(\frac{q_T}{m_H}\right) f_{\rm run}\left[\frac{q_T}{m_H}, \frac{1}{m_H}\mu_*\left(\frac{b_0}{b_T}, \frac{\mu_X^{\rm min}}{2^{w_{\rm FO}} f_{\rm vary}^{v_{\mu_X}}}\right)\right], \\ &\quad \text{for } \mu_X \in \{\mu_B, \mu_S, \nu_S\}, \\ \mu_f &= 2^{w_F} m_H f_{\rm run}\left[\frac{q_T}{m_H}, \frac{1}{m_H}\mu_*\left(\frac{b_0}{b_T}, \frac{\mu_f^{\rm min}}{2^{w_F}}\right)\right], \\ \mu_0 &= \mu_*\left(\frac{b_0}{b_T}, \mu_0^{\rm min}\right). \end{aligned} \tag{A6}$$

Resummation uncertainties are gauged by varying the exponents v_{μ_B}, v_{ν_B}, v_{μ_S}, and v_{ν_S} about their central values $v_i = 0$ by ± 1. The function

$$f_{\rm vary}(x) = \begin{cases} 2(1 - x^2/x_3^2) & 0 \le x \le x_3/2, \\ 1 - 2(1 - x/x_3)^2 & x_3/2 < x \le x_3, \\ 1 & x_3 \le x, \end{cases} \tag{A7}$$

with $x \equiv q_T/m_H$ controls the size of the variations, ranging from a factor of 2 for $x = 0$ to 1 for $x \ge x_3$. Note that both the resummation itself and the associated resummation uncertainty is deactivated for $q_T \ge x_3 m_H$. The combined resummation uncertainty $\Delta_{\rm res}$ is calculated by enveloping 36 variations of suitable combinations of the v_i. For details, we refer the reader to Ref. [55].

For the fixed-order uncertainty $\Delta_{\rm FO}$, we vary $\mu_{\rm FO}$ by a factor of 2 by taking $w_{\rm FO} = \{-1, 0, +1\}$ everywhere. A separate uncertainty Δ_{μ_f} is related to the DGLAP running of the PDFs, for which we vary the PDF scale μ_f by taking $w_F = \{-1, 0, +1\}$. In the nonsingular and fixed-order cross sections, this corresponds to taking $\mu_f \equiv \mu_F = 2^{w_F} m_H$. The resulting $\Delta_{\rm FO}$ and Δ_{μ_f} are then given by the maximum envelope of the respective variations. Finally, a matching uncertainty $\Delta_{\rm match}$ is obtained by varying x_2 in the range [0.2, 0.6].

The total perturbative uncertainty for exclusive quantities is obtained by quadrature sum of the individual contributions, viz.

$$\Delta^2_{\rm total} = \Delta^2_{\rm FO} + \Delta^2_{\rm res} + \Delta^2_{\mu_f} + \Delta^2_{\rm match}. \tag{A8}$$

For inclusive quantities, we instead take the conventional 7-point scale variation band.

APPENDIX B: PLUS DISTRIBUTIONS

Following Ref. [57], we define plus distributions of dimensionless arguments as

$$\begin{aligned} \mathcal{L}_n(x) &\equiv \left[\frac{\Theta(x)\ln^n x}{x}\right]_+ \\ &= \lim_{\beta\to 0}\left[\frac{\Theta(x-\beta)\ln^n x}{x} + \delta(x-\beta)\frac{\ln^{n+1}\beta}{n+1}\right], \end{aligned} \tag{B1}$$

$$\begin{aligned} \mathcal{L}^a(x) &\equiv \left[\frac{\Theta(x)}{x^{1-a}}\right]_+ \\ &= \lim_{\beta\to 0}\left[\frac{\Theta(x-\beta)}{x^{1-a}} + \delta(x-\beta)\frac{x^a - 1}{a}\right]. \end{aligned} \tag{B2}$$

Solutions to the evolution equations for $\mathcal{T}_1^{p_T}$ are conveniently expressed in terms of the function $\mathcal{V}_a(x)$, which is defined as

$$\begin{aligned} \mathcal{V}_a(x) &\equiv \frac{e^{-\gamma_E a}}{\Gamma(1+a)}[a\mathcal{L}^a(x) + \delta(x)], \\ \mathcal{V}_a(k,\mu) &\equiv \frac{1}{\mu}\mathcal{V}_a\left(\frac{k}{\mu}\right). \end{aligned} \tag{B3}$$

The $\mathcal{V}_a$ satisfy a number of useful identities,

$$\int {\rm d}k' \mathcal{V}_a(k',\mu)\mathcal{V}_b(k-k',\mu) = \mathcal{V}_{a+b}(k,\mu), \tag{B4}$$

$$\mathcal{V}_a(k,\mu) = \left(\frac{\mu'}{\mu}\right)^a \mathcal{V}_a(k,\mu'), \tag{B5}$$

$$\mu\frac{\rm d}{{\rm d}\mu}\mathcal{V}_a(k,\mu) = -a\mathcal{V}_a(k,\mu). \tag{B6}$$

APPENDIX C: ONE-LOOP EXPRESSIONS FOR $\mathcal{T}_1^{p_T}$ SOFT, BEAM AND JET FUNCTIONS

Each of the soft, beam and jet functions admits a perturbative expansion in α_s of the form

$$F = \sum_{n=0}^{\infty}\left(\frac{\alpha_s}{4\pi}\right)^n F^{(n)} \tag{C1}$$

for $F \in \{S, B, J\}$. Furthermore, the beam function can be

written as a convolution between the normal parton distribution functions and perturbative kernels as

$$B_i\left(k,x,\mu,\frac{\nu}{\omega}\right)=\sum_m\int_x^1\frac{\mathrm{d}z}{z}\mathcal{I}_{im}\left(k,z,\mu,\frac{\nu}{\omega}\right)f_m\left(\frac{x}{z},\mu\right) \tag{C2}$$

where it is the kernels $\mathcal{I}$ that possess an expansion in α_s.

The one-loop expressions necessary for the $\mathcal{T}_1^{p_T}$ beam function at NLL′ are given by

$$\mathcal{I}_{im}^{(1)}(z)=\delta_{im}\delta(1-z)L_B^\mu(2C_i\Gamma_0L_B^\nu+\gamma_{\mu,B}^{i(0)})-2L_B^\mu P_{im}^{(0)}(z)+I_{im}^{(1)}(z), \tag{C3}$$

$$I_{gq}^{(1)}(z)=z, \tag{C4}$$

$$I_{qq}^{(1)}(z)=1-z, \tag{C5}$$

$$I_{qg}^{(1)}(z)=2z(1-z), \tag{C6}$$

where the logarithms are defined as

$$L_B^\mu=\ln\frac{\mu}{k},\qquad L_B^\nu=\ln\frac{\nu}{\omega}. \tag{C7}$$

The quark and gluon jet functions at one loop are given by

$$J_q^{(1)}(k,\mu,\nu)=C_F\left[\left(7-\frac{2\pi^2}{3}-6\log 2\right)\delta(k)+\left(6+8\log\frac{\nu}{Q}\right)\mathcal{L}_0\left(k,\frac{\mu}{Q}\right)\right] \tag{C8}$$

and

$$J_g^{(1)}(k,\mu,\nu)=\left[C_A\left(\frac{25}{12}-\frac{2\pi^2}{3}\right)+\beta_0\left(\frac{17}{12}+2\log 2\right)\right]\delta(k)+\left[2\beta_0+8C_A\log\frac{\nu}{Q}\right]\mathcal{L}_0\left(k,\frac{\mu}{Q}\right). \tag{C9}$$

The soft function at one-loop order was calculated in Ref. [63]. While the full expression is rather lengthy (and can be found in that reference after setting $\beta=\gamma=1$), the term proportional to $\delta(k_S)$ is given by

$$s_\kappa^{(1)}=-(C_a+C_b+C_J)\frac{\pi^2}{6}-2C_J\log^2 R_J[2+\Theta(R_J-1)] \tag{C10}$$

where we have neglected power-suppressed terms in R_J^2. These have been shown to have at worst a moderate numerical impact, even for values of the jet radius R_J up to 1.5 [63].

APPENDIX D: SPLITTING MAPPINGS AND SPLITTING FUNCTIONS

We report in this section the explicit expressions for the splitting mappings $\bar{\Phi}_N(\Phi_{N+1})$ and splitting functions $\mathcal{P}_{N\to N+1}(\Phi_{N+1})$ used to obtain the results presented in this paper. If we call i and j the two closest partons in the phase space point Φ_{N+1} according to some distance measures, and k the parton obtained by clustering i and j together in the phase space point $\bar{\Phi}_N(\Phi_{N+1})$, all the splitting functions used in the paper take the form

$$\mathcal{P}_{N\to N+1}(\Phi_{N+1})=\begin{cases}f_j^a(x_a,\mu_F)f_{p_b}^b(x_b,\mu_F)\mathcal{P}_{kj}^{\mathrm{ISRA}}(\Phi_{N+1}) & \text{if } k \text{ is ISRA}\\ f_{p_a}^a(x_a,\mu_F)f_j^b(x_b,\mu_F)\mathcal{P}_{kj}^{\mathrm{ISRB}}(\Phi_{N+1}) & \text{if } k \text{ is ISRB}\\ f_{p_a}^a(x_a,\mu_F)f_{p_b}^b(x_b,\mu_F)\mathcal{P}_{jk}^{\mathrm{FSR}}(\Phi_{N+1}) & \text{if } k \text{ is FSR,}\end{cases} \tag{D1}$$

where $f_p^h(x_h,\mu_F)$ is the PDF for the parton p in the hadron h (a or b) with fraction of momentum x_h at factorization scale μ_F, and $\mathcal{P}_{kj}^{\mathrm{ISRA}}(\Phi_{N+1})$, $\mathcal{P}_{kj}^{\mathrm{ISRB}}(\Phi_{N+1})$ and $\mathcal{P}_{jk}^{\mathrm{FSR}}(\Phi_{N+1})$ are three functions whose explicit expressions depend on the splitting mappings and are provided in the following sections. The labels p_a and p_b identify the partons extracted from the first and second beam [if those are not the partons that undergo the splitting, their flavor will not change between Φ_{N+1} and $\bar{\Phi}_N(\Phi_{N+1})$]. To obtain the results presented in this paper, we have used the distance measures given in Eq. (15). Since Eq. (15) does not distinguish emissions coming from different ISR legs, we call ISRA the emissions with positive rapidity and ISRB those with negative rapidity in the reference frame obtained by longitudinally boosting the laboratory frame to the frame where the color singlet has zero rapidity.

1. 1 → 0 mapping

The $1\to 0$ mapping $\bar{\Phi}_0(\Phi_1)$ used in this paper is the one that preserves

(1) The mass of the color singlet.
(2) The rapidity of the color singlet.

The resolution variable used for the $0\to 1$ splitting is the transverse momentum q_T of the color singlet. Furthermore, after calling p_1 the momentum of the emitted parton i, in the ISRA case, we define

$$z=\frac{\sqrt{S}\bar{x}_a}{\sqrt{S}\bar{x}_a+p_1^-}, \tag{D2}$$

while in the ISRB case

$$z=\frac{\sqrt{S}\bar{x}_b}{\sqrt{S}\bar{x}_b+p_1^+}, \tag{D3}$$

where $\bar{x}_a$ and $\bar{x}_b$ are the fractions of momentum carried by the two initial partons in the $\bar{\Phi}_0(\Phi_1)$ phase space point, and $\sqrt{S}$ is the collider energy. We notice that, in the collinear limit, the above definition of z coincides with the energy ratio between the partons k and j. At this point, we can use a single function

$$\mathcal{P}_{kj}^{\mathrm{ISR}}(\Phi_1) = \frac{8\pi\alpha_s(\mu_R)}{q_T^2}(1-z)P_{jk}^{\mathrm{AP}}(z). \tag{D4}$$

to cover both the ISRA and ISRB cases, with the implicit understanding that the definition of z is different between the two cases. The functions are the azimuthally integrated unregulated Altarelli-Parisi splitting functions

$$P_{qq}^{\mathrm{AP}}(z) = C_F\frac{1+z^2}{1-z} \tag{D5}$$

$$P_{qg}^{\mathrm{AP}}(z) = C_F\frac{1+(1-z)^2}{z} \tag{D6}$$

$$P_{gq}^{\mathrm{AP}}(z) = T_F[z^2+(1-z)^2] \tag{D7}$$

$$P_{gg}^{\mathrm{AP}}(z) = 2C_A\left[\frac{z}{1-z}+\frac{1-z}{z}+z(1-z)\right]. \tag{D8}$$

2. 2 → 1 ISR mapping

We define the $2 \to 1$ ISR mapping $\bar{\Phi}_1(\Phi_2)$ as the one that preserves

(1) The momentum q of the color singlet.
(2) The rapidity η_1 of the final-state parton that does not come from the splitting.

The resolution variable used for the $1 \to 2$ ISR splitting is

$$\mathcal{T}_1 = p_{2T}, \tag{D9}$$

where p_2 the momentum of the emitted parton i, and, similarly to what we did above, in the ISRA case, we define

$$z = \frac{\sqrt{S}\bar{x}_a}{\sqrt{S}\bar{x}_a + p_2^-} \tag{D10}$$

while in the ISRB case

$$z = \frac{\sqrt{S}\bar{x}_b}{\sqrt{S}\bar{x}_b + p_2^+}, \tag{D11}$$

where $\bar{x}_a$ and $\bar{x}_b$ are the fractions of momentum carried by the two initial partons in the $\bar{\Phi}_1(\Phi_2)$ phase space point, and $\sqrt{S}$ is the collider energy. Similarly to what we did above, we then define

$$\mathcal{P}_{kj}^{\mathrm{ISR}}(\Phi_2) = \frac{8\pi\alpha_s(\mu_R)}{\mathcal{T}_1^2}(1-z)P_{jk}^{\mathrm{AP}}(z). \tag{D12}$$

3. 2 → 1 FSR mapping

We define the $2 \to 1$ FSR mapping $\bar{\Phi}_1(\Phi_2)$ as the one that preserves

(1) The momentum q of the color singlet.
(2) The rapidity η_1 of the final-state parton with the largest transverse momentum.

The resolution variable used for the $1 \to 2$ FSR splitting is

$$\mathcal{T}_1 = \sqrt{\frac{p_{T2}}{p_{T1}}(p_1+p_2)^2}, \tag{D13}$$

where p_2 is the momentum of the emitted parton i and p_1 that of the other final-state parton j. Furthermore, we define

$$z = \frac{p_{1T}}{p_{1T}+p_{2T}}. \tag{D14}$$

We notice that, in the collinear limit, the above definition of z coincides with the energy ratio between the partons j and k. This is the first FSR splitting we encounter in the calculation. We define

$$\mathcal{P}_{kj}^{\mathrm{FSR}}(\Phi_2) = \frac{8\pi\alpha_s(\mu_R)}{\mathcal{T}_1^2}\frac{1-z}{z}P_{kj}^{\mathrm{AP}}(z). \tag{D15}$$

4. Second 2 → 1 FSR mapping

In GENEVA, we make use of two different kind of splitting mappings. The $\bar{\Phi}_N(\Phi_{N+1})$ mappings are used above the r_N resolution cut to spread the r_N resummed distribution over the differential Φ_{N+1} events, while the $\tilde{\Phi}_N(\Phi_{N+1})$ mappings are used below the r_N resolution cut to subtract the infrared divergences of the Φ_{N+1} events at small r_N. Since the two mappings are used on complementary subsets of the $d\Phi_{N+1}$ phase space, they do not need to coincide, although they did in fact coincide in all the previous GENEVA implementations. In this paper, however, using the same FSR mappings above and below the $\mathcal{T}_1$ resolution cut would have resulted in significant complications in their computational implementations. For this reason, we made use of a different FSR $2 \to 1$ $\tilde{\Phi}_1(\Phi_2)$ mapping, defined as the one that preserves

(1) The momentum q of the color singlet.
(2) The rapidity η_{12} of the final-state jet (given by the two clustered partons in Φ_2).

This choice allows for a simpler treatment of the standard ξ, y, and ϕ variables used when dealing with the subtraction of the infrared diveregences, since they are typicallly defined in terms of energies and angles of the emitted

parton p_2 with respect to the emitter $p_1 + p_2$. On the other hand, the $\bar{\Phi}_1(\Phi_2)$ mapping proves more convenient when the splitting function is written in terms of $\mathcal{T}_1$, as defined in Eq. (D13), which depends separately on p_{1T} and p_{2T}.

5. Impact of the choice of the splitting mapping

In the GENEVA formalism, the choice of the splitting mapping and the resolution variables affects the way the so-called splitting functions are implemented (see Sec. 3.1 of Ref. [21] for the technical details). These are used to determine the event weights in a way that guarantees that the generated events are distributed according to the resummed spectrum in the given resolution variable (in this case, the transverse momentum of the Higgs boson). The way GENEVA achieves this requires dividing each event weight by the cross section (approximated in the collinear limit) at a given underlying phase space point Φ_N (determined by the splitting mapping) and value of the resolution variable r_N. This approach requires computing the integration limits for the splitting variables at fixed Φ_N and r_N, and the feasibility of such a calculation significantly limits the number of new mappings that can be implemented.

In the work presented in this paper, the expression of the $\mathcal{T}_1^{p_T}$ resolution variable makes the implementation of alternative splitting mappings very complicated. To nevertheless investigate the expected uncertainty associated with the choice of the mapping, we have performed a dedicated study using the existing implementation of the Drell-Yan process, where the standard N-jettiness [see Eq. (12) of the draft] was used as resolution variable and two different splitting mappings are currently available. The results of the comparison are shown in Fig. 11. Both the splitting mappings here preserve the resolution variable $\mathcal{T}_0$, but one of them (corresponding to the red distributions in the figure) also preserves the transverse momentum of the vector boson. From the ratio plot in the lower pane, we can see that the numerical impact associated with the choice of the different mappings appears to be below 5% across the entire spectrum and within the theoretical uncertainty estimated through scale variations.

APPENDIX E: EFFECT OF SCALE SETTING CHOICES ON THE q_T SPECTRUM

In Fig. 10 we show the Higgs boson q_T spectrum in $b\bar{b} \to H$ for spectrum (blue) and cumulant (red) scale settings. These different scale choices were discussed in detail in Sec. V A. We observe that both spectra are in good agreement in the peak and the tail region. In particular for the tail of distribution, this behavior is expected as both distributions are matched to the same fixed-order prediction and therefore must agree in the fixed-order limit. In the transition region, however, the higher order terms have a significant effect which can be as large as 40%. The large size of this effect is peculiar to the $b\bar{b} \to H$ process, and its origin is discussed in detail in Ref. [34].

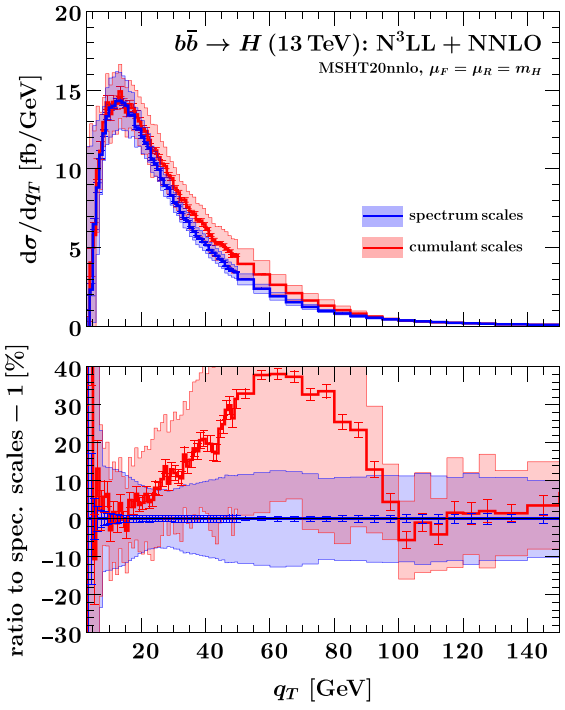


FIG. 10. Parton-level Higgs boson q_T spectrum in $b\bar{b} \to H$ for spectrum and cumulant scale settings.

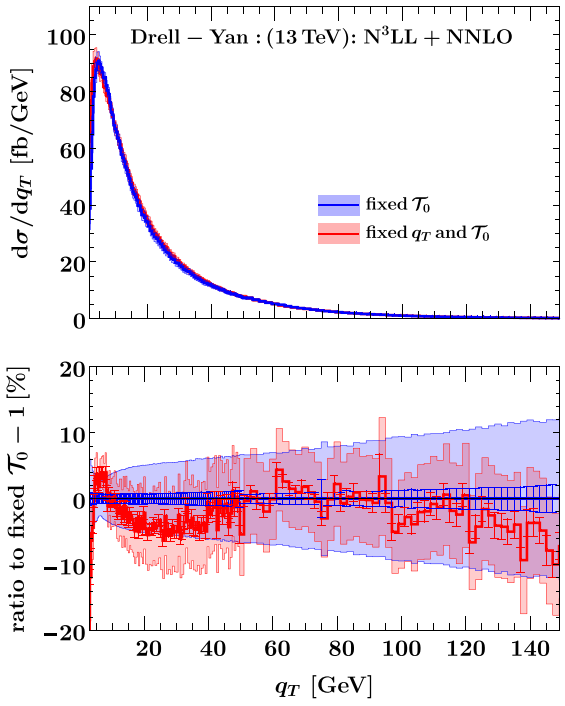


FIG. 11. Transverse momentum spectrum of the vector boson for the Drell-Yan process with different splitting mappings.

APPENDIX F: FLAVOR STRUCTURE OF GENEVA

The GENEVA method is sufficiently general that a number of different choices for the resolution variables r_0 and r_1 may be made, each resulting in an NNLO + PS accurate generator. To date, choices for r_0 include the transverse momentum of the color singlet q_T, the $0-$jettiness $\mathcal{T}_0$ and the hardest jet transverse momentum $p^j_{1,T}$, while choices for r_1 include the conventional $1-$jettiness $\mathcal{T}_1$, the second jet transverse momentum $p^j_{2,T}$ and, as of this work, the $1-$jettiness with transverse momentum measures $\mathcal{T}_1^{p_T}$. It is clear that the number of different permutations now available may cause confusion when one wishes to refer to a specific implementation of GENEVA. Inspired by the origins of the term "flavor" in particle physics (due to Gell-Mann), we therefore propose a nomenclature which should serve to clarify exactly which choice of resolution variables has been made in a given case. This appears in Table II.

TABLE II. Flavors of GENEVA implementation.

Flavor	r_0	r_1	Reference
Vanilla (V)	$\mathcal{T}_0$	$\mathcal{T}_1$	[13]
Raspberry ripple (RR)	q_T	$\mathcal{T}_1$	[24]
Tutti frutti (TF)	$p^j_{1,T}$	$p^j_{2,T}$	[27]
Mint choc chip (MCC)	q_T	$\mathcal{T}_1^{p_T}$	This work

[1] G. Billis, B. Dehnadi, M. A. Ebert, J. K. L. Michel, and F. J. Tackmann, Phys. Rev. Lett. **127**, 072001 (2021).
[2] X. Chen, T. Gehrmann, E. W. N. Glover, A. Huss, B. Mistlberger, and A. Pelloni, Phys. Rev. Lett. **127**, 072002 (2021).
[3] X. Chen, T. Gehrmann, E. W. N. Glover, A. Huss, P. F. Monni, E. Re, L. Rottoli, and P. Torrielli, Phys. Rev. Lett. **128**, 252001 (2022).
[4] X. Chen, P. Jakubčík, M. Marcoli, and G. Stagnitto, Phys. Lett. B **869**, 139804 (2025).
[5] S. Alioli, C. W. Bauer, C. Berggren, A. Hornig, F. J. Tackmann, C. K. Vermilion, J. R. Walsh, and S.Zuberi, J. High Energy Phys. 09 (2013) 120.
[6] P. F. Monni, P. Nason, E. Re, M. Wiesemann, and G. Zanderighi, J. High Energy Phys. 05 (2020) 143.
[7] J. M. Campbell, S. Höche, H. T. Li, C. T. Preuss, and P. Skands, Phys. Lett. B **836**, 137614 (2023).
[8] B. K. El-Menoufi, C. T. Preuss, L. Scyboz, and P. Skands, J. High Energy Phys. 11 (2025) 045.
[9] M. Dasgupta, F. A. Dreyer, K. Hamilton, P. F. Monni, G. P. Salam, and G. Soyez, Phys. Rev. Lett. **125**, 052002 (2020).
[10] M. van Beekveld *et al.*, Phys. Rev. Lett. **134**, 011901 (2025).
[11] F. Herren, S. Höche, F. Krauss, D. Reichelt, and M. Schoenherr, J. High Energy Phys. 10 (2023) 091.
[12] S. Höche, F. Krauss, and D. Reichelt, Phys. Rev. D **111**, 094032 (2025).
[13] S. Alioli, C. W. Bauer, C. Berggren, F. J. Tackmann, and J. R. Walsh, Phys. Rev. D **92**, 094020 (2015).
[14] I. W. Stewart, F. J. Tackmann, and W. J. Waalewijn, Phys. Rev. Lett. **105**, 092002 (2010).
[15] S. Alioli, A. Broggio, S. Kallweit, M. A. Lim, and L. Rottoli, Phys. Rev. D **100**, 096016 (2019).
[16] S. Alioli, A. Broggio, A. Gavardi, S. Kallweit, M. A. Lim, R. Nagar, D. Napoletano, and L. Rottoli, J. High Energy Phys. 04 (2021) 254.
[17] S. Alioli, A. Broggio, A. Gavardi, S. Kallweit, M. A. Lim, R. Nagar, D. Napoletano, and L. Rottoli, J. High Energy Phys. 04 (2021) 041.
[18] S. Alioli, A. Broggio, A. Gavardi, S. Kallweit, M. A. Lim, R. Nagar, and D. Napoletano, Phys. Lett. B **818**, 136380 (2021).
[19] T. Cridge, M. A. Lim, and R. Nagar, Phys. Lett. B **826**, 136918 (2022).
[20] S. Alioli, G. Billis, A. Broggio, A. Gavardi, S. Kallweit, M. A. Lim, G. Marinelli, R. Nagar, and D. Napoletano, J. High Energy Phys. 06 (2023) 205.
[21] S. Alioli, G. Billis, A. Broggio, A. Gavardi, S. Kallweit, M. A. Lim, G. Marinelli, R. Nagar, and D. Napoletano, J. High Energy Phys. 05 (2023) 128.
[22] I. W. Stewart, F. J. Tackmann, and W. J. Waalewijn, Phys. Rev. D **81**, 094035 (2010).
[23] S. Alioli, A. Broggio, and M. A. Lim, J. High Energy Phys. 01 (2022) 066.
[24] S. Alioli, C. W. Bauer, A. Broggio, A. Gavardi, S. Kallweit, M. A. Lim, R. Nagar, D. Napoletano, and L. Rottoli, Phys. Rev. D **104**, 094020 (2021).
[25] P. F. Monni, E. Re, and P. Torrielli, Phys. Rev. Lett. **116**, 242001 (2016).
[26] W. Bizon, P. F. Monni, E. Re, L. Rottoli, and P. Torrielli, J. High Energy Phys. 02 (2018) 108.
[27] A. Gavardi, M. A. Lim, S. Alioli, and F. J. Tackmann, J. High Energy Phys. 12 (2023) 069.
[28] I. W. Stewart, F. J. Tackmann, J. R. Walsh, and S. Zuberi, Phys. Rev. D **89**, 054001 (2014).
[29] P. Cal, M. A. Lim, D. J. Scott, F. J. Tackmann, and W. J. Waalewijn, J. High Energy Phys. 03 (2025) 155.
[30] P. Nason, J. High Energy Phys. 11 (2004) 040.
[31] M. A. Ebert, J. K. L. Michel, F. J. Tackmann *et al.*, Report No. DESY-17-099, Deutsches Elektronen-Synchrotron DESY, 2018, http://scetlib.desy.de.
[32] A. Banfi, G. P. Salam, and G. Zanderighi, J. High Energy Phys. 03 (2005) 073.
[33] L. Buonocore, M. Grazzini, J. Haag, L. Rottoli, and C. Savoini, Phys. Rev. D **106**, 014008 (2022).
[34] P. Cal, R. von Kuk, M. A. Lim, and F. J. Tackmann, Phys. Rev. D **110**, 076005 (2024).

[35] C. Biello, A. Sankar, M. Wiesemann, and G. Zanderighi, Eur. Phys. J. C **84**, 479 (2024).
[36] C. Biello, J. Mazzitelli, A. Sankar, M. Wiesemann, and G. Zanderighi, J. High Energy Phys. 04 (2025).088.
[37] F. Bishara, U. Haisch, P. F. Monni, and E. Re, Phys. Rev. Lett. **118**, 121801 (2017).
[38] J. C. Collins and D. E. Soper, Nucl. Phys. **B193**, 381 (1981); **B213**, 545(E) (1983).
[39] J. C. Collins and D. E. Soper, Nucl. Phys. **B197**, 446 (1982).
[40] J. C. Collins, D. E. Soper, and G. F. Sterman, Nucl. Phys. **B250**, 199 (1985).
[41] S. Catani, D. de Florian, and M. Grazzini, Nucl. Phys. **B596**, 299 (2001).
[42] D. de Florian and M. Grazzini, Nucl. Phys. **B616**, 247 (2001).
[43] J. Collins, *Foundations of Perturbative QCD* (Cambridge University Press, Cambridge, England, 2013), Vol. 32.
[44] C. W. Bauer, S. Fleming, and M. E. Luke, Phys. Rev. D **63**, 014006 (2000).
[45] C. W. Bauer, S. Fleming, D. Pirjol, and I. W. Stewart, Phys. Rev. D **63**, 114020 (2001).
[46] C. W. Bauer and I. W. Stewart, Phys. Lett. B **516**, 134 (2001).
[47] C. W. Bauer, D. Pirjol, and I. W. Stewart, Phys. Rev. D **65**, 054022 (2002).
[48] C. W. Bauer, S. Fleming, D. Pirjol, I. Z. Rothstein, and I. W. Stewart, Phys. Rev. D **66**, 014017 (2002).
[49] T. Becher and M. Neubert, Eur. Phys. J. C **71**, 1665 (2011).
[50] M. G. Echevarria, A. Idilbi, and I. Scimemi, J. High Energy Phys. 07 (2012) 002.
[51] J.-Y. Chiu, A. Jain, D. Neill, and I. Z. Rothstein, J. High Energy Phys. 05 (2012) 084.
[52] Y. Li, D. Neill, and H. X. Zhu, Nucl. Phys. **B960**, 115193 (2020).
[53] J.-y. Chiu, A. Jain, D. Neill, and I. Z. Rothstein, Phys. Rev. Lett. **108**, 151601 (2012).
[54] M. A. Ebert and F. J. Tackmann, J. High Energy Phys. 02 (2017) 110.
[55] M. A. Ebert, J. K. L. Michel, I. W. Stewart, and F. J. Tackmann, J. High Energy Phys. 04 (2021) 102.
[56] G. Billis, F. J. Tackmann, and J. Talbert, J. High Energy Phys. 03 (2020) 182.
[57] Z. Ligeti, I. W. Stewart, and F. J. Tackmann, Phys. Rev. D **78**, 114014 (2008).
[58] R. Abbate, M. Fickinger, A. H. Hoang, V. Mateu, and I. W. Stewart, Phys. Rev. D **83**, 074021 (2011).
[59] G. Lustermans, J. K. L. Michel, F. J. Tackmann, and W. J. Waalewijn, J. High Energy Phys. 03 (2019) 124.
[60] G. Billis, J. K. L. Michel, and F. J. Tackmann, J. High Energy Phys. 02 (2025) 170.
[61] A. J. Larkoski, D. Neill, and J. Thaler, J. High Energy Phys. 04 (2014) 017.
[62] I. W. Stewart, F. J. Tackmann, J. Thaler, C. K. Vermilion, and T. F. Wilkason, J. High Energy Phys. 11 (2015) 072.
[63] D. Bertolini, D. Kolodrubetz, D. Neill, P. Pietrulewicz, I. W. Stewart, F. J. Tackmann, and W. J. Waalewijn, J. High Energy Phys. 07 (2017) 099.
[64] J. Thaler and K. Van Tilburg, J. High Energy Phys. 03 (2011) 015.
[65] J. Thaler and K. Van Tilburg, J. High Energy Phys. 02 (2012) 093.
[66] A. Banfi, G. P. Salam, and G. Zanderighi, J. High Energy Phys. 08 (2004) 062.
[67] T. Becher and M. Neubert, J. High Energy Phys. 07 (2012) 108.
[68] T. Becher, M. Neubert, and L. Rothen, J. High Energy Phys. 10 (2013) 125.
[69] A. Gavardi, Next-to-next-to-leading order predictions for diboson production in hadronic scattering combined with parton showers, Ph.D. thesis, Università degli Studi di Milano-Bicocca, Italy, Milan Bicocca University, 2023.
[70] S. Bailey, T. Cridge, L. A. Harland-Lang, A. D. Martin, and R. S. Thorne, Eur. Phys. J. C **81**, 341 (2021).
[71] R. L. Workman *et al.* (Particle Data Group), Prog. Theor. Exp. Phys. **2022**, 083C01 (2022).
[72] R. V. Harlander, S. Liebler, and H. Mantler, Comput. Phys. Commun. **184**, 1605 (2013).
[73] S. Alioli, G. Billis, A. Broggio, and G. Stagnitto, J. High Energy Phys. 01 (2026) 065.
[74] R. Boughezal, J. M. Campbell, R. K. Ellis, C. Focke, W. Giele, X. Liu, F. Petriello, and C. Williams, Eur. Phys. J. C **77**, 7 (2017).
[75] R. Mondini and C. Williams, J. High Energy Phys. 05 (2021) 045.
[76] S. Dulat, T.-J. Hou, J. Gao, M. Guzzi, J. Huston, P. Nadolsky, J. Pumplin, C. Schmidt, D. Stump, and C. P. Yuan, Phys. Rev. D **93**, 033006 (2016).
[77] T. Sjöstrand, S. Mrenna, and P. Z. Skands, Comput. Phys. Commun. **178**, 852 (2008).
[78] B. Cabouat and T. Sjöstrand, Eur. Phys. J. C **78**, 226 (2018).
[79] P. F. Monni, E. Re, and M. Wiesemann, Eur. Phys. J. C **80**, 1075 (2020).
[80] Z. Nagy and D. E. Soper, J. High Energy Phys. 06 (2014) 097.
[81] M. Dasgupta, F. A. Dreyer, K. Hamilton, P. F. Monni, and G. P. Salam, J. High Energy Phys. 09 (2018) 033; 03 (2020) 083(E).
[82] G. Bewick, S. Ferrario Ravasio, P. Richardson, and M. H. Seymour, J. High Energy Phys. 04 (2020) 019.
[83] J. R. Forshaw, J. Holguin, and S. Plätzer, J. High Energy Phys. 09 (2020) 014.
[84] K. Hamilton, R. Medves, G. P. Salam, L. Scyboz, and G. Soyez, J. High Energy Phys. 03 (2021) 041.
[85] V. Chekhovsky *et al.* (CMS Collaboration), Nature (London) **652**, 321 (2026).
[86] S. Alioli, G. Bell, G. Billis, A. Broggio, B. Dehnadi, M. A. Lim, G. Marinelli, R. Nagar, D. Napoletano, and R. Rahn, Phys. Rev. D **109**, 094009 (2024).
[87] G. Bell, R. Rahn, and J. Talbert, J. High Energy Phys. 07 (2019) 101.
[88] G. Bell, R. Rahn, and J. Talbert, J. High Energy Phys. 09 (2020) 015.
[89] G. Bell, B. Dehnadi, T. Mohrmann, and R. Rahn, J. High Energy Phys. 07 (2024) 077.
[90] F. J. Tackmann, J. High Energy Phys. 08 (2025) 098.
[91] M. A. Lim and R. Poncelet, Phys. Rev. D **112**, L111901 (2025).